CHALMERS
UNIVERSITY OF TECHNOLOGY

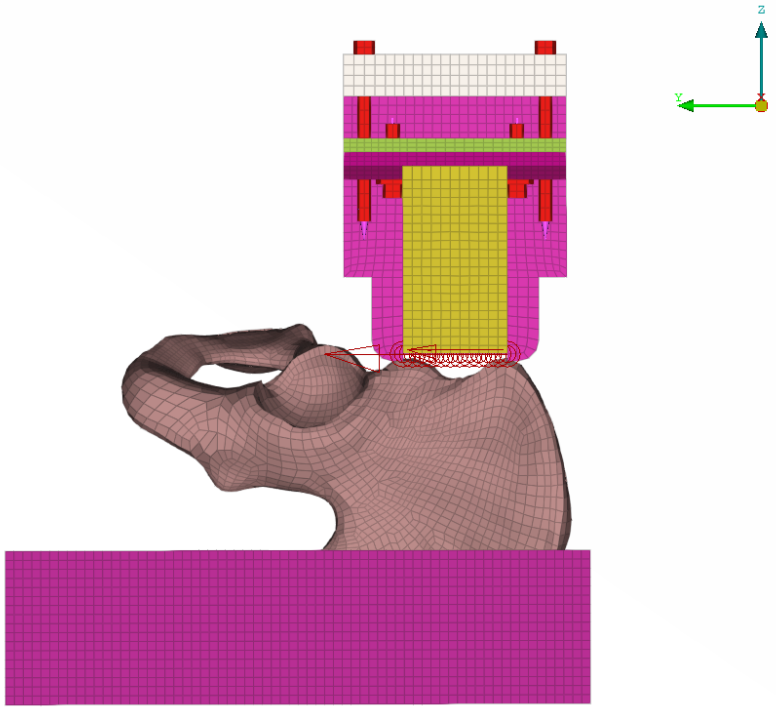

Iliac wing fracture from lap belt loading

Master's thesis in Applied Mechanics

Shreeraksha Umapathi Bhat

DEPARTMENT OF MECHANICS AND MARITIME SCIENCES

CHALMERS UNIVERSITY OF TECHNOLOGY
Gothenburg, Sweden 2024
www.chalmers.se

Master's thesis 2024

Iliac wing fracture from lap belt loading

Shreeraksha Umapathi Bhat

CHALMERS
UNIVERSITY OF TECHNOLOGY

Department of Mechanics and Maritime Sciences
Division of Vehicle Safety
Injury Prevention
Chalmers University of Technology
Gothenburg, Sweden 2024

Iliac wing fracture from lap belt loading
Shreeraksha Umapathi Bhat

Supervisor: Erik Brynskog, Division of Vehicle Safety, Chalmers
Co-supervisor: Bengt Pipkorn, Autoliv Development AB
Examiner: Johan Iraeus, Division of Vehicle Safety

Master's Thesis 2024
Department of Mechanics and Maritime Sciences
Division of Vehicle Safety
Injury Prevention
Chalmers University of Technology
SE-412 96 Gothenburg
Telephone +46 31 772 1000

Cover: Iliac wing fracture test setup.

Typeset in LaTeX
Printed by Chalmers Reproservice
Gothenburg, Sweden 2024

Iliac wing fracture from lap belt loading
Shreeraksha Umapathi Bhat
Department of Mechanics and Maritime Sciences
Chalmers University of Technology

Abstract

Autonomous cars are expected to increase in the near future and one of the features of those cars is to ride reclined as the driving task is managed by the vehicle. In the reclined posture the occupant will have a more horizontal torso position. With the current 3- point seatbelt it is more difficult to control torso body motion in reclined postures compared to upright postures and the risk of submarining may also increase. Submarining is an event where the pelvis slips under the lap belt and loads the abdomen instead of the pelvis. There are different techniques to avoid submarining and one of them is to increase the pre-tension force in the lap belt. This avoids the risk of submarining but instead, the risk of iliac wing fracture increases due to the higher pelvis load. Recently experiments on isolated iliac wings have been performed,with the intention to find the fracture load. In this thesis, these experiments were recreated in a simulation environment and with those simulation results, the injury risk functions are generated to estimate the probability of the iliac wing fracture. A conclusive single injury risk function suitable for practical application could not be determined.

Keywords: Submarining, pelvis injury, iliac wing fracture, injury risk function.

List of Acronyms

Below is the list of acronyms that have been used throughout this thesis listed in alphabetical order:

AIIS	Anterior Inferior Iliac Spine
ASIS	Anterior Superior Iliac Spine
AIC	Akaike Information Criteria
ATD	Anthropomorphic Test Devices
FEM	Finite Element Method
IRF	Injury Risk Function

Contents

List of Figures

List of Tables

1
Introduction

.

1.1 Background

Road traffic injuries are estimated to be the eighth leading cause of death worldwide for all ages and the foremost cause of mortality for children and adolescents aged 5 to 29 [1]. According to the world health organization (WHO) 1.35 million people die every year due to traffic accidents [2] and someone dies on the road every 24 seconds [3]. Furthermore, 20-50 million people have non-fatal injuries and many are disabled as a result of their injuries [2]. The UN views preventing these injuries as a crucial problem for sustainable development. Research on road safety aims to reduce accidents in general, particularly fatalities and injuries [4]. According to Sweden's vision zero, no one should die or sustain permanent disabilities as a result of a traffic accident and the solution for this is not to prevent the accidents but instead find the solution to minimize the injuries happening in accidents [5].

1.2 Evolution of testing methods

To improve vehicle safety, it is critical to understand the mechanics of impact in diverse collision scenarios. In the early 1950s, cadavers, animals, and volunteers were used as test subjects, but due to ethical issues and insufficient repeatability, mechanical test dummies were developed known as anthropomorphic test devices (ATDs) see figure 1.1. These dummies aim to be biofidelic (approximate response of humans), robust, repeatable, reproducible, and instrumented, and these properties will help to predict injuries. Virtual counterparts of these crash test dummies have been integrated into FE simulations to execute crash scenarios within a virtual setting. This approach was adopted to reduce the time and costs associated with conducting physical crash tests and to facilitate more comprehensive examinations of diverse crash scenarios encompassing a wide range of crash characteristics. Subsequently, Finite Element - Human Body Models (FE-HBMs) were developed to enhance the biofidility of human body responses and generate more precise injury predictions. In conjunction with ATDs and FE-HBMs, one valuable tool for estimating the likelihood of injuries is the Injury Risk Function (IRF). The IRF provides insights into the probability of sustaining an injury under specific loading conditions.

Figure 1.1: Example of Anthropomorphic test device [50]

1.3 Motivation

By 2030, the number of autonomous cars will grow by a factor of ten[35] and one of the possible features could be that drivers can recline the seats to various angles according to occupant's comfort [6]. However, there are many risks associated with it and one of them is submarining [7].

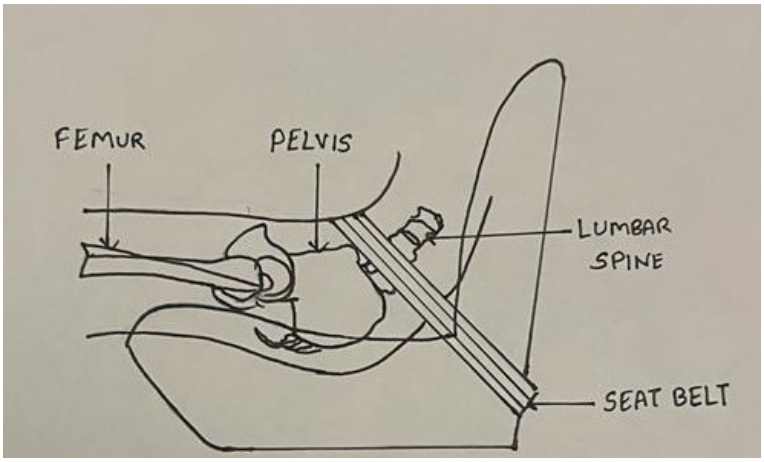

Figure 1.2: Event of submarining

Submarining is an event where the pelvis slips under the lap belt as seen in figure 1.2. As a consequence, the abdomen will be loaded instead of the pelvis. The

abdomen being the soft tissue cannot withstand the loading of the seat belt during the higher severity crashes. Various methods are still under research for reducing the submarining risk in reclined seats and some of them are; increasing the pre-tensioning force in the lap belt, adding an anti-submarining ramp and adjusting its position in the front of the seat [34], and using knee bolsters [33]. By increasing the pre-tensioning force in the lap belt, submarining can be avoided but, the iliac wings could get fractured due to high pelvis load. This has been shown in multiple other submarining-related experiments and was confirmed by experiments performed at the University of Virginia(UVA) [30]. To further analyze these injuries, a follow-up experiment was designed where the dynamics of the impact were removed to only focus on the belt loading aspects. The experiment was carried out at two levels, at first isolated seated non-impact pull was carried out with four cadavers to know the iliac wing deformation at this condition. Two out of four cadavers experienced an iliac wing fracture in the region between ASIS(anterior superior iliac spine) and AIIS(anterior inferior iliac spine) [31]. To understand these fractures in more detail, a simplified test setting was used in the second level. In this thesis, the experiments of the second level will be replicated using simulations.

1.3.1 Aim

The aim of this thesis is to predict the iliac wing fracture risk and develop an IRF for the iliac wing fracture from the lap belt loading.

1.3.2 Objective

To fulfil the aim, the iliac wing loading experiment will be re-created using FE simulations. Subject-specific iliac wing geometries will be generated and simulated. The specific parameter for the IRF will be chosen after evaluating the results of the simulations.

1.3.3 Limitations

The limitations of this thesis are,

- Only the fracture at the anterior superior iliac spine is considered.
- Only load from the lap belt is considered while developing the IRF.
- The analysis will be done with an existing pelvis model [17].
- The progressive fracture won't be simulated.
- No additional experiments are done for the generation of the data.

2

Theory

This chapter covers the fundamental anatomy of the pelvis and gives an overview of the different methods used in the thesis such as the Finite Element Method(FEM), and survival analysis.

2.1 Finite Element Method

FEM is a numerical approach to solve partial differential equations(PDE) in an approximate manner and it is used to solve a number of engineering problems [8]. In FEM, a given domain is considered as a collection of subdomains known as elements, and the governing equation is estimated across each element using any of the classic variational methods or any method that is acceptable [9]. Then the elements are assembled and the dynamic equilibrium equation is solved. The matrix form of the dynamic equilibrium equation is represented in equation 2.1

$$\boldsymbol{M}\ddot{\boldsymbol{u}}^n + \boldsymbol{C}\dot{\boldsymbol{u}}^n + \boldsymbol{K}\boldsymbol{u}^n = \boldsymbol{f}^n \tag{2.1}$$

where $\boldsymbol{M}$ is the global mass matrix, $\boldsymbol{C}$ is the global damping matrix, $\boldsymbol{K}$ is the global stiffness matrix, $\ddot{\boldsymbol{u}}$ is the acceleration vector, $\dot{\boldsymbol{u}}$ is the velocity vector, $\boldsymbol{u}$ is the displacement vector and $\boldsymbol{f}$ is the load vector. n denotes the current time step.

The equation 2.1 is solved by the solver using explicit or implicit time integration. The main difference between both methods is an approach to time incrementation. In an implicit method, at every time step global equilibrium has to be achieved i.e., at every time step the system of equations is solved therefore each time step has to be kept longer due to this the computation time is longer. In an explicit method, it is not required to converge each step but the time step has to be kept small in order to get good results. The equation 2.2 and 2.3 represent the explicit and implicit methods respectively. The implicit method uses the current and later states to solve the equation whereas the explicit uses the current and previous states to solve.
Explicit time integration:

$$u^{n+1} = f(u^n, \dot{u}^n, \ddot{u}^{n-1}, \dot{u}, \ddot{u}^{n-1}, ...) \tag{2.2}$$

Implicit time integration:

$$u^{n+1} = f(\dot{u}^{n+1}, \ddot{u}^{n+1}, u^n, \dot{u}^n, \ddot{u}^n, ...) \tag{2.3}$$

The solver automatically identifies the minimum time step required for the simulation in case of the explicit analysis and it is limited by the critical time step. The equation 2.4 represents the formula the solver uses to calculate the critical time step.

$$\Delta t_{critical} = \frac{l_e}{c_e} \qquad c_e \approx \sqrt{\frac{E_e}{\rho_e}} \tag{2.4}$$

where l_e is the element length, E_e is the young's modulus and ρ_e is the density. Critical time will be calculated for each element and if the critical time is not satisfied for a particular element non-physical mass will be added to that element to satisfy the critical time step. According to guidelines the added mass should not be greater than 5% and it is followed in this project as well.
Figure 2.1 tells which method is suitable for different engineering problems. As it is seen in the graph, when the loading speed and loading amplitude are higher, explicit FEM is the best suitable method, and when the loading speed is less, the implicit method is usually preferred. In this project, the explicit solver LS-Dyna (R12.1.0) is used due to the high loading speed and non-linear response.

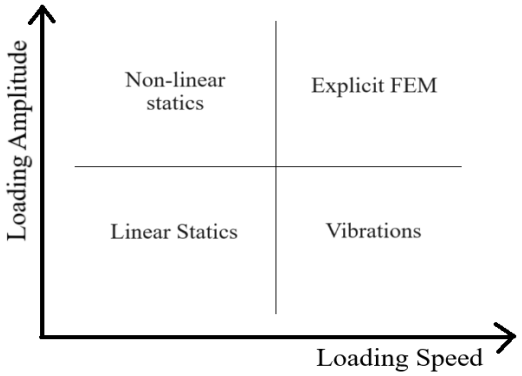

Figure 2.1: Implicit and Explicit FEM

2.1.1 Mesh and mesh quality

In FEM, the domain is discretized into a number of finite elements. The basic classification of elements are beams, shells, solids, and discrete elements represented in figure 2.2. Beam elements are 1D elements with a defined cross-section, shell elements are modelled as a mid surface with thickness offset, and solid elements represent the complete volume of the geometry[11].

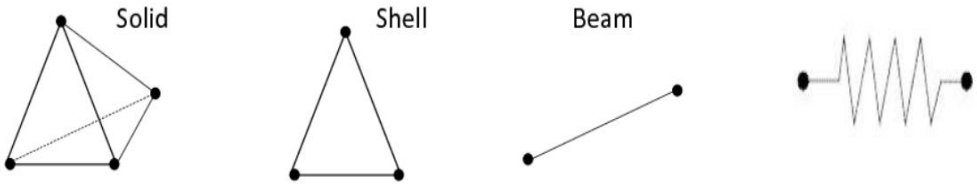

Figure 2.2: Different types of elements

The quality of these elements plays a very important role in getting good results from the FE model. The quality criteria listed below in table 2.1 and illustrated in 2.3 apply to all of the shell elements generated by the models used in this project.

	Aspect ratio[-]	Skewness [^{o}]	Warping [^{o}]	Jacobian [-]	Min angle quads [^{o}]	Max angle quads[^{o}]
Calculation	PATRAN	PATRAN	PATRAN	ANSA	IDEAS	IDEAS
	<10	<60	<20	>0.3	>20	<120

Table 2.1: Mesh quality criteria

The aspect ratio is the ratio between the maximum and minimum characteristic dimensions of the element. It is given by, AR = $\frac{max(l_i)}{min(l_i)}$ for i=1,2,3.., where l is the length of the element[12].

The degree of skewness indicates how closely an element resembles an ideal element. It is calculated as, skewness = 90 - min(θ_i) for i=1,2,3.., where θ represents the angle between the line joining the midpoints of the opposite sides[13].

Warp angle is a measure of how distant an element is from being planar. For a quadrilateral element, it is calculated as W = arcsin($\frac{h}{e}$) W is the waring angle, h is the distance between the nodes and the reference plane and e is the shortest edge [14].

Jacobian is the determinant of the jacobian matrix. Jacobian matrix maps the natural coordinate system to the cartesian coordinate system. It is the measure of the distortion of the element. A perfect element will have the jacobian of 1.

Min angle and max angle are the measures between two neighbouring facets. It should be greater than 20^o and less than 120^o.

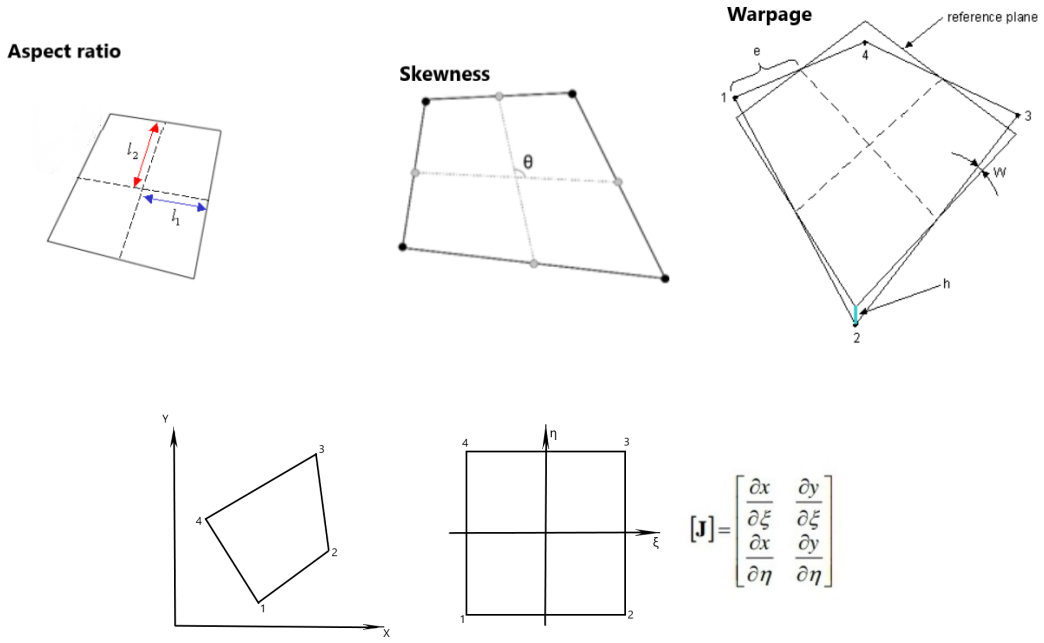

Figure 2.3: Illustration of the quality criteria of the FEM elements

2.2 Bone

The main mechanical properties of bones are that they are viscoelastic, inhomogeneous, anisotropic, and nonlinear. Cortical bone, also referred to as compact bone, forms the outer layer of the majority of bones. It provides structural support and provides a rigid framework for muscles for movements. The osteons are cylindrical structural units connected together to form compact bone and acts as reinforcements to the matrix that provides tensional strength. The osteons are aligned with the expected direction of force and help the bone to resist bending. Each osteon consists of lamellae, which are extracellular matrices around the bone vessels and nerve fiber. Lamellea is made up of organic and inorganic materials. The lamellae are responsible for the hardness and rigidity of the bone. The inner layer, referred to as trabecular bone is porous, and 20% of the skeleton is made up of trabecular bone [45]. The trabecular bone consists of trabeculae and they are arranged along the stress lines. Cortical bone is characterized by its dense and solid structure, which gives it a higher density when compared to the trabecular bone which has marrow-filled cavities[15]. The cortical bones are stiffer and can withstand more stress but less strain, whereas the trabecular bone being more porous can withstand more strain before failure than compact bone [36]. The basic types of bone fracture are represented in figure 2.4. The different types of fractures mentioned in the figure 2.4 are linear, oblique displaced, spiral, greenstick and oblique non displaced respectively.

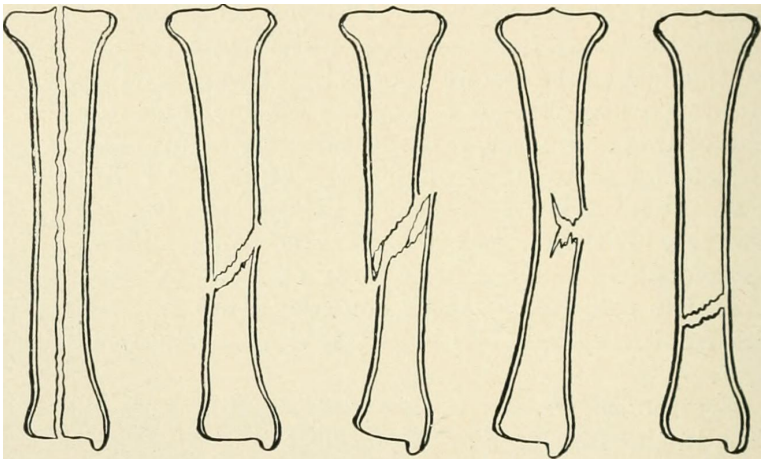

Figure 2.4: Different types of bone fracture [47]

2.3 Anatomy of the pelvis

The pelvis represented in figure 2.5 is a bony structure at the base of the spine that connects the abdomen to the lower extremities. It consists of the sacrum, the coccyx, the ischium, the ilium, and the pubis. The sacrum is a triangular-shaped bone located in the rear of the pelvis, below the lumbar vertebrae. It is made up of five fused vertebrae (S1-S5) and comprises the posterior section of the pelvic girdle. The sacrum links the spine to the hip bones and aids in the transmission of weight from the upper body to the lower extremities. The coccyx, often known as the tailbone, is a tiny, triangular bone found at the base of the sacrum. The coccyx acts as an attachment location for ligaments and muscles but does not act as a weight carrier.

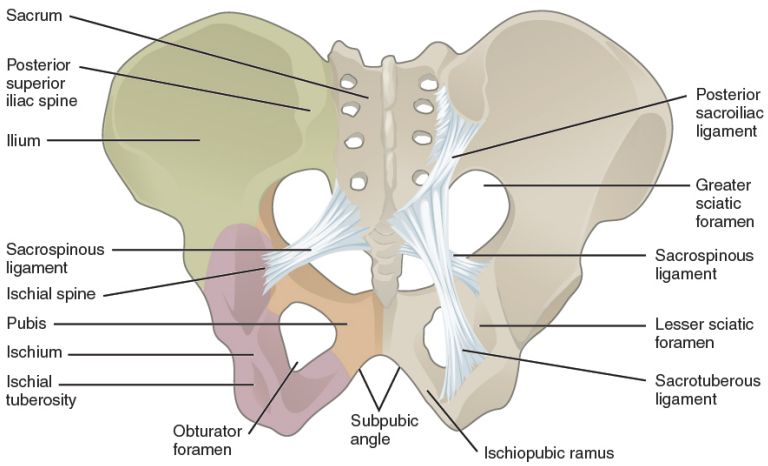

Figure 2.5: Anatomy of pelvis [48]

The three bones, the ischium, ilium, and pubis, together known as the innominate bone represented in figure 2.6. The iliac crest is the top edge of the ilium from the anterior superior iliac spine (ASIS) to the posterior superior iliac spine (PSIS). The ASIS is the anterior (front) aspect of the illium and the PSIS is the posterior (back)

aspect. The anterior inferior iliac spine (AIIS) is positioned on the anterior of the illium, inferior (below) and medial to the ASIS. The ridge going from the ASIS to the AIIS is called the iliac spine which was loaded in the present project.

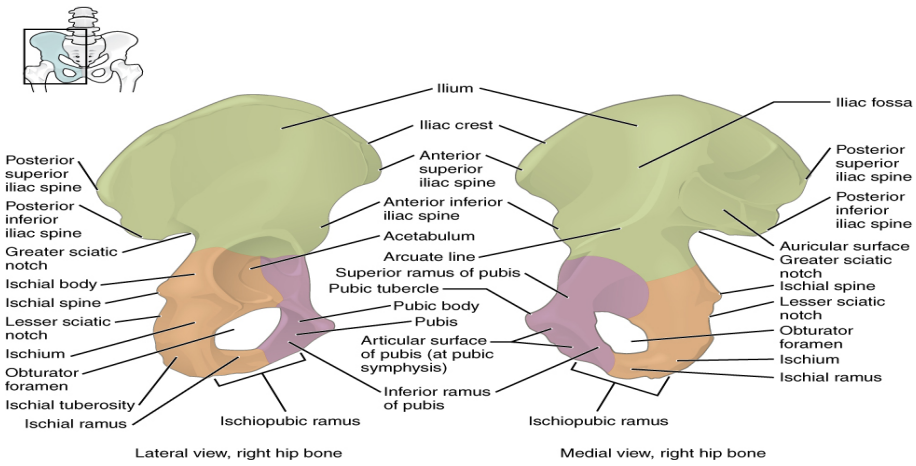

Figure 2.6: Iliac wing [49]

2.4 Injury and injury mechanism of pelvis

Pelvic fractures are a major factor leading to fatalities and long-term disabilities in motor vehicle collisions [19] and they rank as the third most prevalent AIS2+ injury [20]. The most common kind of pelvic injury in automotive accidents is caused by lateral impacts, such as a pedestrian being hit by a car or the occupants in a side crash [18]. The lateral impacts mainly cause the fracture of the pubic rami and acetabulum [21]. The lateral impacts will cause lateral compression or vertical shear of the pelvis [21]. The available data for frontal impacts is limited [18] when it comes to categorizing fracture types for the pelvis, but based on the limited information, it was observed that fractures primarily occurred on the iliac wings [22].

2.5 Survival analysis

Survival analysis is a statistical method that can be described as the time until an event occurs [23]. In biomechanical cases, the event is generally considered as death. Survival analysis, as a regression approach, has a unique quality that distinguishes it from other regression models i.e. it can efficiently handle censored data [24]. Censoring data involves the classification of data in specific ways. Various types of censoring exist, including left, right, interval, and exact censoring. Left censoring refers to situations where an event has taken place, but the exact time is unknown. Right censoring occurs when an event has not yet occurred. Interval censoring involves events that have taken place within an interval of time. Exact censoring is applied when an event has occurred and the corresponding time is known. In this particular project, fractures are considered as events. When the exact timing of a fracture is known, it is classified as exact censoring. Left censoring, on the other

hand, pertains to situations where a fracture has occurred but the precise timing remains unknown. Conversely, right censoring is applied when a fracture does not occur at all.

With the capacity to handle covariates, survival analysis makes it possible to investigate how different variables, like age, affect survival time. These covariates, also known as predictors, can be of various forms. Multiple categorical predictors like different treatments, continuous predictors like age, or binary predictors like sex [24]. The approach for predicting survival based on the predictors varies depending on the method employed. Different methods like parametric, semi-parametric, or non-parametric methods can be employed.

The non-parametric method is a statistical technique that does not make any assumptions about the sample's characteristics (parameters) or the nature of the observed data, whether it is quantitative or qualitative. The Kaplan-Meier method is a type of non-parametric estimator. The parametric method, on the other hand, assumes that the data follows a specific distribution. The different distributions used generally for parametric survival analysis are the exponential, Weibull, log-normal, and log-logistic. A semi-parametric model will have both parametric and non-parametric components. The Cox regression model is a semi-parametric model.

Survival analysis is usually done using parametric distribution as it is easier to describe and it allows multivariate regression. It is important to evaluate when selecting the specific parametric distribution for survival analysis, to see how well the distribution fits the dataset and to compare one or more distributions to select the best one. In this project, the Akaike's Information Criteria (AIC) is used for selecting the distribution. AIC is a mathematical technique used to evaluate the goodness of fit of a model. It is used to compare the different distributions and determine which best fits the data. It is defined as,

$$AIC = 2k - 2ln(\hat{L}) \tag{2.5}$$

where k is the number of estimated parameters in the model and $\hat{L}$ is the maximum value of the likelihood function for the model [24]. The best-fit distribution is the one with minimum AIC value [25].

2.6 Injury risk function

The IRF depicts the likelihood of sustaining a certain injury at a given mechanical load level. These IRFs are widely used while designing vehicle safety systems and evaluating their effectiveness [26]. The different steps for generating IRFs are, collecting the relevant data, assigning the censoring, estimating the distribution parameters, checking the distribution assumption, choosing the distribution, and calculating the 95% confidence interval [27]. A confidence interval gives a range where we think a certain number (like an average) lies for the whole population, based on our sample data. The confidence level (like 95%) is how sure we are that

this range includes the true value [28]. It is recommended to only have one curve per body region, injury type, and injury severity [27].

3
Methods

This study is carried out with a series of steps, starting with modelling the experimental setup and validating the test rig characteristics. Following this, the subject-specific iliac wing models were created. Finally, an IRF was generated from the simulation results. The modelling was carried out in ANSA (Beta CAE Systems) version (v22.1.5), LS Dyna (LST, Livermore, CA, USA) version R12.1 was used as a solver and LS PrePost (4.9) was to post-process the data. Data analysis is done using MATLAB (Natick, Massachusetts) version (R2021b). The statistical analysis and generation of IRFs are carried out using R software (Natick, Massachusetts) version (4.2.2).

3.1 Input data

As mentioned earlier in this thesis the experiments done in UVA [30][31][52][53] was replicated using simulations. In the experiment, to investigate the fracture tolerance of the ilaic wings, a component-level iliac wing test is done by converting the more complex loading of the whole body belt pull environment to a more simplified loading environment [51]. For this component level test 22 iliac wings were used. To carry out this thesis, the UVA has shared the experimental test results, photos, videos of the experiment, sketch of the experimental setup, CT scan of the ilaic wing in the potting cup and the CT scan of the iliac wings which are cleaned is provided in the .stl format.

3.2 Modeling of the Belt fork

A belt fork was used to apply the load on the pelvises. The sketch of the belt fork was given and the 3D model was done using CATIA V5. The model was imported into ANSA for pre-processing. Figure 3.1 represents the complete fork modelled in ANSA. Some simplifications were done when modelling in ANSA compared to the experimental setup. In the experiment, the seat belt is clamped between the bottom and the top clamp plates i.e. the seat belt first passes through the top of the bottom clamp plate and then it exits from the bottom of the top clamp plate and is left as a free end. As it is difficult to model looping through the clamping plates because it requires the belt to bend and slide over each 90^o corner while being compressed by clamping plates and also, the 90^o contact angle between the seatbelt and clamping plates is difficult to model. Due to these reasons, the seatbelt is tied to the top of the bottom-most clamping plate. The fork tine, clamping plates, top

plate, and reinforced plate were modelled using under integrated constant hexa solid stress elements, and MAT1 MAT_ELASTIC material card is used. Fork tine, the top plate, and the reinforced plate are of steel which has an Elastic modulus of 210 GPA, a density of 7.85e^{-6} kg/mm^3, and a Poisson ratio of 0.3. Clamping plates are of cold-rolled steel and have an Elastic modulus of 208 GPa, a density of 8.856e^{-6} kg/mm^3, and a Poisson's ratio of 0.3.

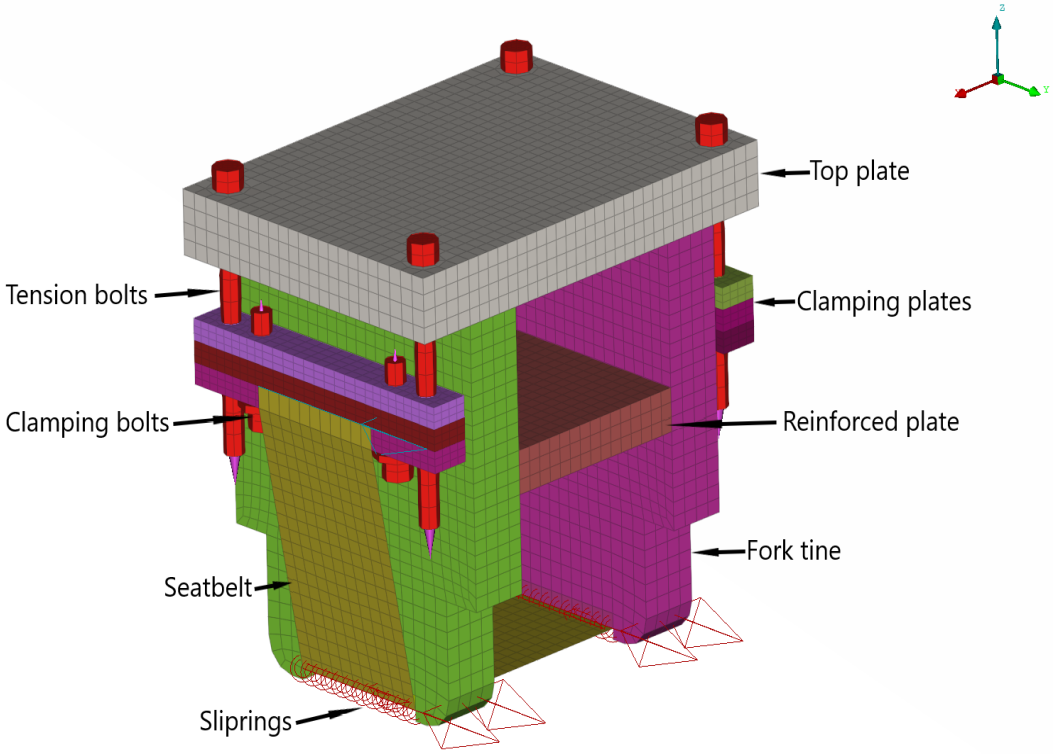

Figure 3.1: Belt fork modeled in ANSA

3.2.1 Modeling of the bolts

The head height and diameter of the bolts are 6.35mm and 9.6mm respectively and meshed wih hexahedral elements. The length of the tension bolts are 76.20mm and the length of the clamping bolts are 25.40 mm. The clamping bolts have a washer and the diameter of the washer is 1.6*head diameter and has 2 mm thickness. The bolts are of grade 8 steel and have an Elastic modulus of 190 Gpa, a density of 7.85e^{-6} kg/mm^3, and a Poisson's ratio of 0.29. The bolts were torqued to 4ft-lbs to provide a consistent starting tension to the seatbelt in the experiment. In the modelling, the pretension stress is given to the bolt. The calculation of the bolt pretension stress is given below.

$$T = K * F * d\left(1 - \frac{L}{100}\right) \tag{3.1}$$

where, T = wrench torque(ft-lbs) = 4 (experimental value)
K = constant that depends on bolt material and size = 0.2 (normal dry mild steel)
d = nominal bolt diameter (ft) = 0.03125
F = axial bolt force (lb)
L = lubrication factor (%) = 0

$$F = \frac{4}{0.2 * 0.03125} = 640lb$$

$F = 2847$N force in each bolt

The torque is the value specified in the experiment, but the resulting axial force is computed from a theoretical formula which is likely not what we will have in the experiment. In addition, we don't know what the belt slip is, how much creep affects the belt load over time, etc. so the computed values were used as a starting point in a calibration study. The calibrated bolt force resulted in 1.8kN and was used in the following simulations

$$Stress = \frac{Force}{Area} \tag{3.2}$$

$$Stress = \frac{1.8(kN)}{32.15(mm^2)} = 0.05625kN/mm^2$$

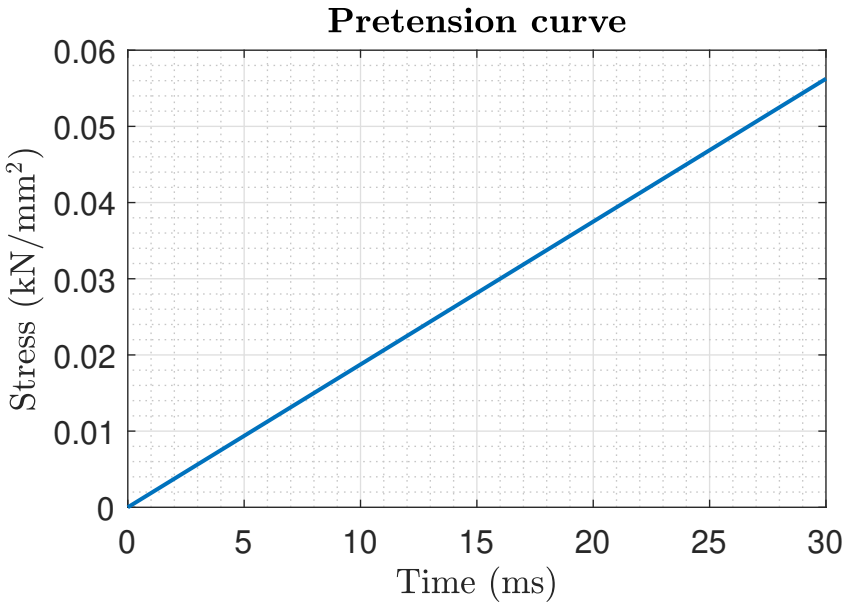

Figure 3.2: Bolt pretension curve

Figure 3.2 represents the curve used in the model for pre-tensioning the bolts. In LS-Dyna, the pre-tensioning force is applied as stress. It reaches the desired stress in 30ms in a linear increase so that the model won't get affected by a lot of dynamics.

3.2.2 Modeling of seatbelt

The seatbelt is modelled using Belytschko-Tsay membrane quad shell elements. Belytschko-Tsay membrane shell elements are fully integrated membrane elements and are best used for fabrics [16]. It has a total of 726 elements. The seatbelt has a thickness of 1.2mm. MAT_B01_MAT_SEATBELT_2D material card was used, see figure 3.3.

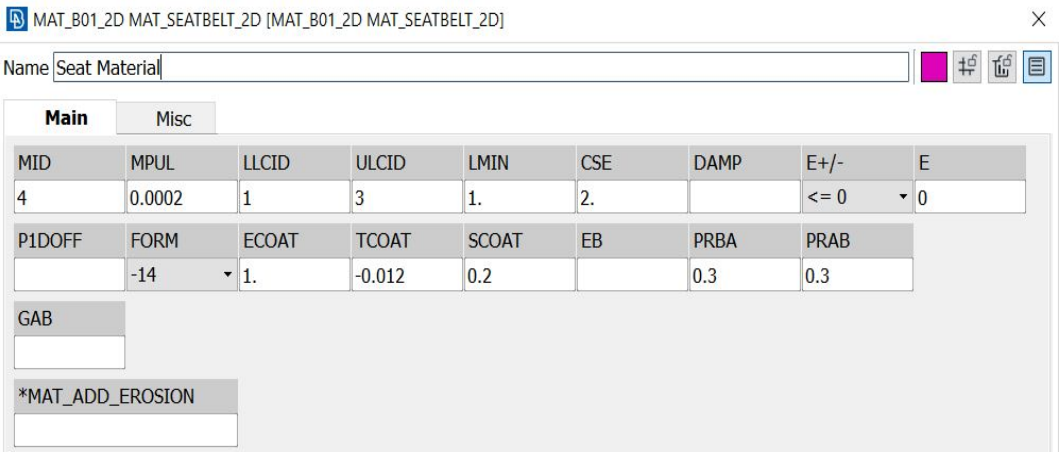

Figure 3.3: Seatbelt material card in ANSA

In the above figure, LLCID and ULCID represent the loading and unloading curves respectively. The initial stiffeness of the belt is 20% at 18.268 kN and due to a lot of unknowns as specified in the previous section, the parameter study is taken place for deciding the stiffeness of the belt to be 20% strain at 10.96 kN. The seatbelt is coated using a sheet of elastic-ideal-plastic material to add bending stiffness to the belt, specified by FORM = -14 in the figure. ECOAT, TCOAT, and SCOAT are Young's modulus, yield stress, and thickness of the coating [38].

3.2.3 Modeling of slip rings

Slip rings are used at the four bottom corners of the fork, as it is very difficult to model the sharp corner contact between the seatbelt and the fork with the current element density. The slip rings are modelled using the ELEMENT_SEATBELT_SLIPRING option in ANSA. The slip rings allow the seatbelt material to slide through the slip rings.

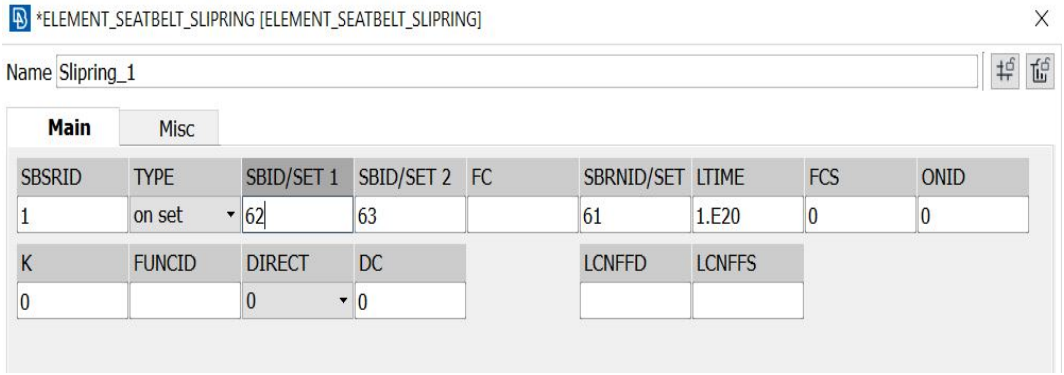

Figure 3.4: ELEMENT_SEATBELT_SLIPRING card in ANSA

Figure 3.4 represents the card for the seatbelt slip ring. SBID represents the element set and SBRNID represents the node set. The two sets are seat belt elements that share common nodes and the node set is coincident with the common nodes of the element set. The node set is the nodes of fork tine and it is not directly connected to the seat belt nodes. The elements and nodes are picked in the same order for the sets. Zero friction was assumed in the slip rings.

3.3 Seat belt characterization test

The seat belt characterization test was done in order to calibrate the fork model. In order to do this, the model was displaced into an aluminium bar. The force-displacement data from the experiments is used as a calibration target.

3.3.1 Modeling of the round bar

The round bar is an aluminium bar which is shown in figure 3.5. The geometry of the aluminium bar was given, and the sketch was done in CATIAV5 and then imported to ANSA.

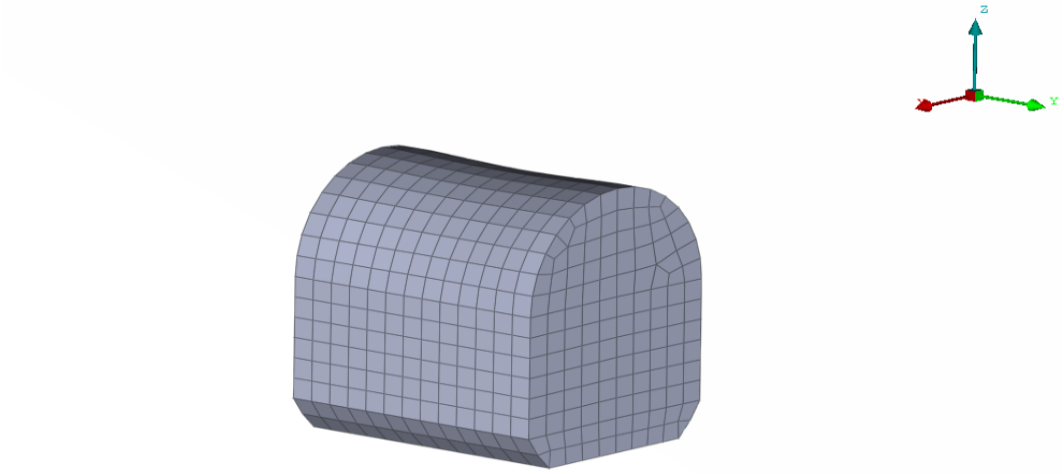

Figure 3.5: Round impactor

3.3.2 Positioning of the bar

The aluminium bar is positioned below the fork, ensuring there is enough space to prevent contact penetration between them. It is aligned so that the center of the seat belt matches the center of the curved part of the bar. However, due to the bar's slightly greater width compared to the seat belt, it is adjusted in the y direction to maintain an equal distance of extension on both sides beyond the seat belt.

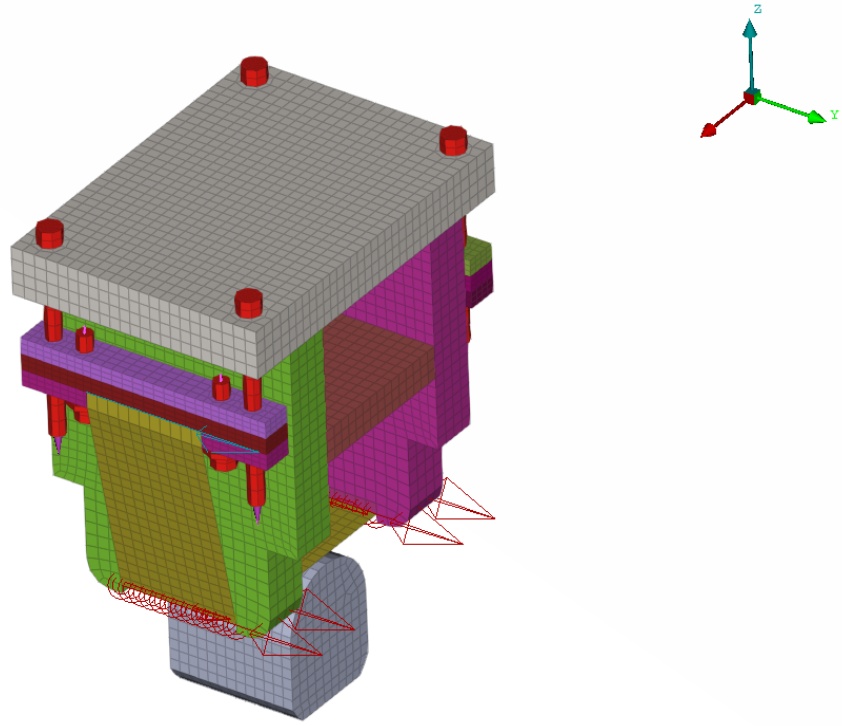

Figure 3.6: Fork and aluminium rod setup

3.3.3 Contact definition

The automatic surface-to-surface contact definition is used to define the contact between the seat belt and aluminium rod. As it is a simple case without any complex geometry, the moving body, which is the seat belt, is designated as the slave, while the body that interacts with the moving body, the aluminum bar, is chosen as the master. The static friction of 0.2 is used for the contact.

3.3.4 Global damping

During the pre-tensioning process of the bolts, the model undergoes significant dynamics due to the rapid application of tension, which occurs within a very short time frame of 30 ms. In order to mitigate some of the noise or excessive dynamics, a global damping effect is introduced for a duration of 30 ms. This damping serves to reduce the oscillations or fluctuations in the system, leading to a more stable and controlled behaviour during the pre-tensioning phase. The model is run without the global damping first to calculate the lowest frequency which has to be damped. The critical mass damping is calculated using the below equation.

$$\text{critical damping} = \frac{4 \times \pi}{T} \tag{3.3}$$

T - Time period - 1.79 ms, time period of the lowest frequency.

$$\text{critical damping} = \frac{4 \times \pi}{1.79} \approx 7$$

In the global damping card, the load curve for the damping has to be specified, so a constant damping value of 7 from 0 to 30 ms curve is defined and the damping is linearly reduced from 30 to 40 ms.

3.3.5 Boundary condition

The boundary-prescribed motion card is used for specifying the boundary conditions. The aluminium bar should be fixed in space without any movement, so all six degrees of freedom should be locked, the figure 3.7 curve is defined to achieve this. The fork should move only in the translational z-direction and the other five degrees of freedom should be locked. For the five degrees of freedom which are locked the curve 3.7 is used.

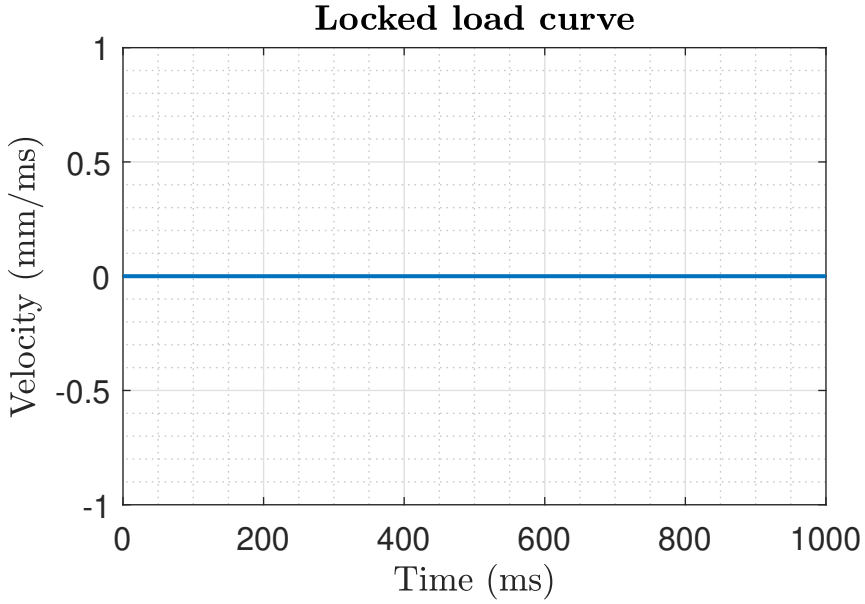

Figure 3.7: Locked load curve

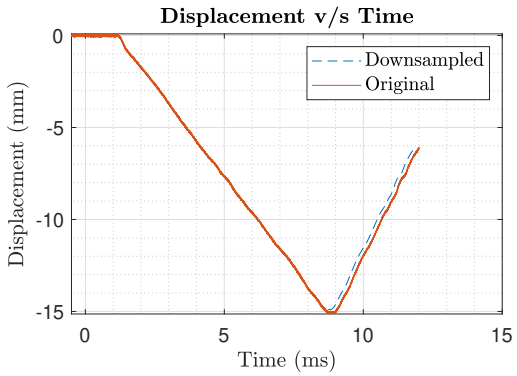

(a) Comparison of original and downsampled displacement of experimental results

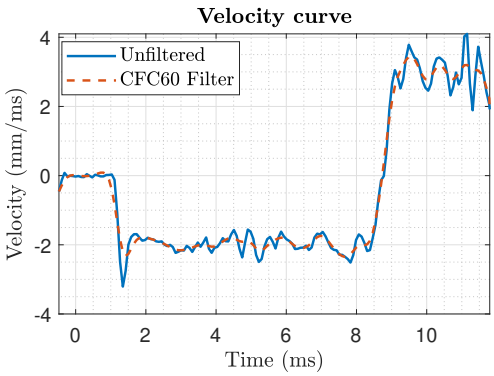

(b) Comparison of the filtered and unfiltered velocity of experimental results

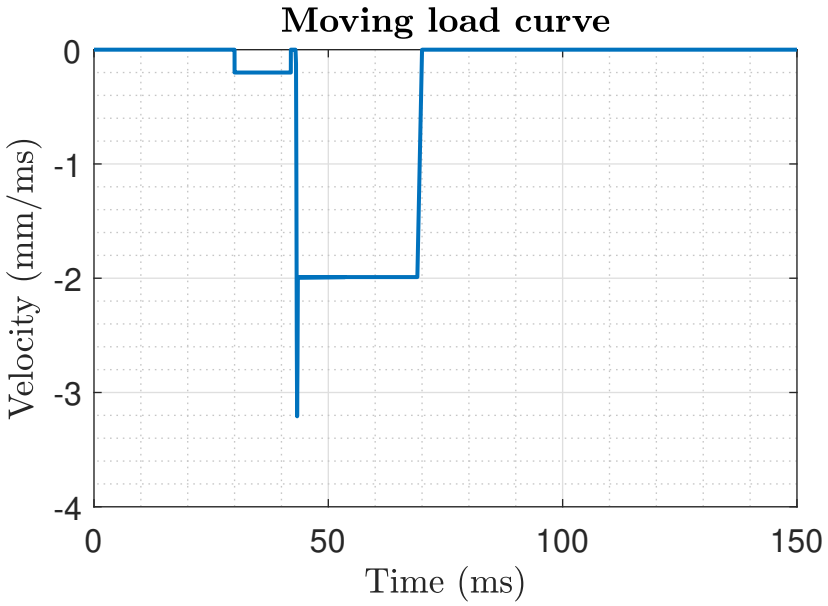

Figure 3.9: Moving load curve

For the translation z movement of the fork, the 3.9 curve is used. During the experiment, in order to ensure a consistent starting position for the load, the fork was set to a force of 10 N at the beginning of each test. In the modelling process, the velocity required to achieve the 10 N force is calculated. The simulation is run without applying the pre-load, and the time at which the force output reaches 10 N is determined. At that specific time, the z displacement of the fork is checked. By the time and displacement values, the velocity needed to reach the 10 N force is calculated as -0.2 mm/ms, and it takes 12 ms to reach the desired force level. So, after the pre-tensioning of the bolts, pre-load is applied from 30 to 42 ms. During the experiment, the seat belt characterization test was performed four times, yielding displacement and time data. Firstly, the average displacement is calculated based on the results from these four tests. However, due to the presence of significant noise in the data, downsampling of the displacement values is conducted. Downsampling is reducing the sample size of the data, here from 31252 data points it is reduced to

200 as seen in the figure 3.8a. Subsequently, the downsampled displacement vector is differentiated with respect to the time vector, resulting in a velocity curve. Despite the downsampling, the velocity curve was still noisy. So, the cfc60 filter is used to remove the peaks from the velocity curve can be seen in figure 3.8b. For further simplification, after the first bump, a straight line is drawn through the data, and this curve is applied from 43 ms which can be seen in the figure 3.9.

3.3.6 Calibration of the model

The results obtained from the baseline values were not matching with the experimental results which is shown in the figure 4.1, so calibration of the model was needed. It is done using the parametric study by varying the bolt pretension force and the seat belt stress-strain data.

3.4 Iliac wing test

In this section, the modeling of the iliac wings, positioning of the wings inside the potting cup, and boundary conditions used in the test are explained in detail.

3.4.1 Modeling of the iliac wings

As previously mentioned, the experiment involved studying 22 iliac wings extracted from 11 cadaver subjects. CT scan was cleaned and was available in .stl format for the pelvis of all 11 subjects. For this project, a pelvis model developed by [17] was utilized. To morph the pelvis model to the CT scan data, two methods were employed: landmarked pelvis and surface matching.

3.4.1.1 Landmarked Pelvis

In this method, they were landmarked to align with the .stl geometries and then optimization was done in Matlab to get the shapes that minimize the error between the landmarks and corresponding points on a statistical model[39]. The resulting landmarked FE models were provided to this thesis by the supervisors.

3.4.1.2 Surface matched Pelvis

The surface-matched pelvis was generated from the landmark matched pelvis models. The cortical bones are modeled using shells and the trabecular bones are modeled using solids. The landmarked shells are first morphed into the CT scan data in ANSA using the Direct morph tool (DFM). Figure 3.10a represents the CT scan data of an individual right iliac wing. Figure 3.10b represents the landmark matched iliac wing and the ct scan wing. As it is seen it is not completely aligned to the CT scan. To align it more accurately DFM tool is used in ANSA and pelvis surface nodes from the landmarked matched versions are projected onto the ct scan data, which is shown in the figure 3.10c. The element quality after using DFM is not always great, especially around the edge of the DFM zone, as is seen in figure 3.11a.

Furthermore, figure 3.10c shows that near the ASIS, AIIS, and iliac crest, which is the area of interest, the nodes are not perfectly aligned with the CT scan. To achieve a more accurate alignment in the regions of interest, manual node selection was performed, and the move grids tool was used to align the nodes with the CT scan data. This alignment process was also applied to improve the element quality, as demonstrated in Figure 3.11b. By employing the move grids tool, both the node alignment and element quality 2.3 were effectively improved, ensuring a more accurate representation of the pelvis in the region of interest.

In order to align the trabecular bone elements, a radial basis morphing MATLAB code is utilized. This code requires three sets of nodes. One "source", one "target", and one "to morph". The source is the landmarked cortical nodes, the target is the aligned cortical nodes and to morph set is the trabecular bone nodes. By this, the shells are moved from the source to the target, and the trabecular bone is forced to follow this movement. The output of this code is saved in .k format which has the trabecular elements which are aligned to the target nodes (morphed). In this process, some elements of the trabecular elements will have bad quality, which is fixed using a fix quality tool or move grid tool.

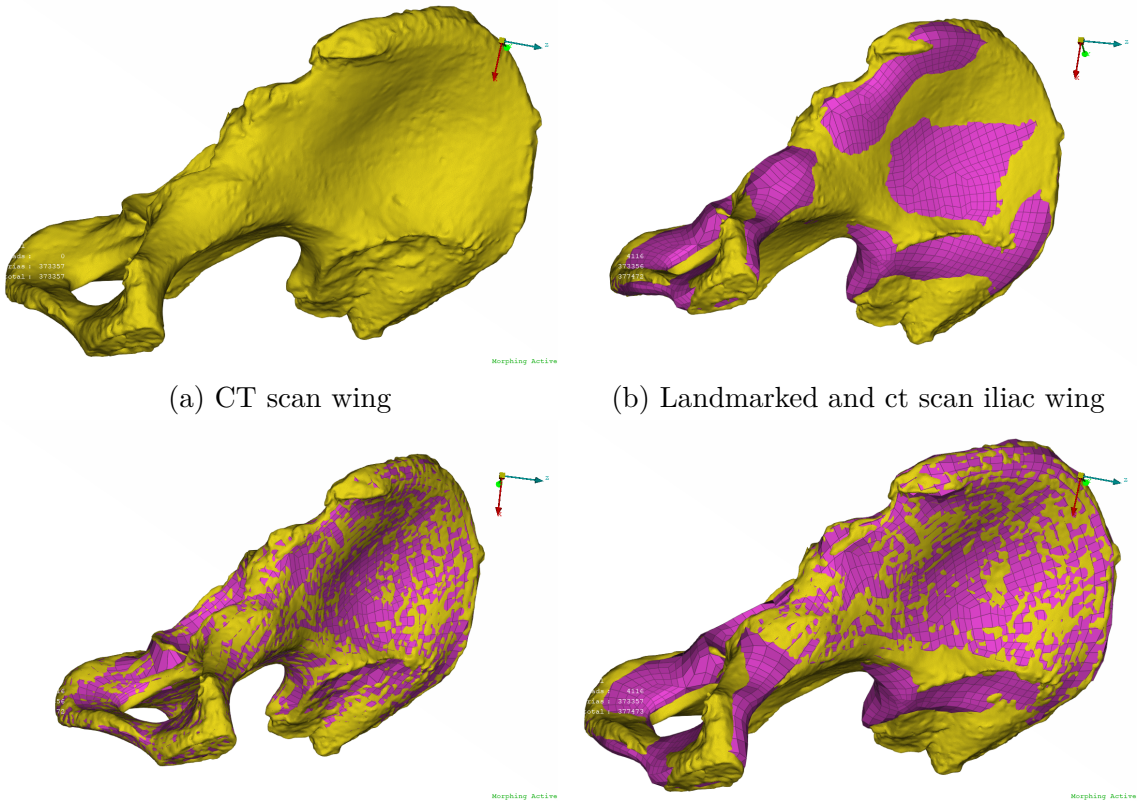

(a) CT scan wing

(b) Landmarked and ct scan iliac wing

(c) Morphed wing using direct morphing

(d) Manually morphed after direct morphing

Figure 3.10: Process of morphing of a right iliac wing of a 999 specimen

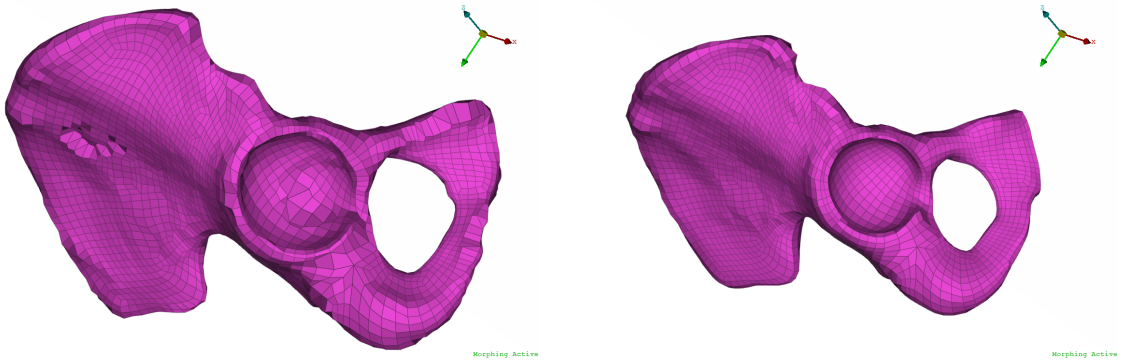

(a) Iliac wing after using DFM (b) Iliac wing after fixing the element quality

Figure 3.11: 999 specimens before and after fixing the element quality

3.4.2 Modeling of the potting cup

The geometry of the potting cup was given, and the sketch was done in CATIAV5 and then imported to ANSA. It is made up of rigid elements. It is filled with constant-stress solid elements(under-integrated). The height of the solid elements depends on the geometry of the iliac wings. The potting cup is filled with the potting material smooth cast which has an Elastic modulus of 0.962 GPa, a density of $1.05e^{-6}$ kg/mm^3, and a Poisson ratio of 0.3 [40].

3.4.3 Positioning of the iliac wing in the potting cup

The CT scan data on how the iliac wing is positioned in the potting cup was available for 11 iliac wings: 713, 714, 715, 716, 999 for both left and right wings, and 792 for the left wing only, but for the other specimens: 798, 990, 997, 998, 1000 for both the left and right wings and 792 for the right wing only the data was missing. The segmented 3D geometries without the potting material were still available for all the specimens. The CT scan data was cleaned and exported in .stl format using 3D slicer software(version 5.2.2).

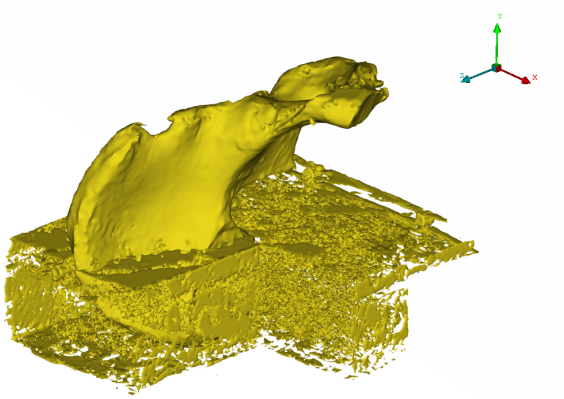

Figure 3.12: CT scan to represent the positioning of an iliac wing (specimen left 714)

Figure 3.13: Roll angle

Figure 3.12 represents the cleaned CT scan imported in ANSA. The FE model iliac wing is positioned on top of the CT scan to get accurate positioning. The depth of the potting cup differs for each specimen and is influenced by its geometry, and from the 3.12 it is seen that the depth of the cup also is determined in a CT scan. In cases where CT scans were not accessible, the positioning of the iliac wing was determined based on the provided roll angle, which indicates the degree of medial bending 3.13, and the depth of the potting cup is assumed by the test photos of the experiment.

Specimen	Left (Degrees)	Right (Degrees)
713	75	90
714	90	90
715	90	75
716	75	90
792	75	90
798	75	75
990	90	75
997	75	75
998	90	75
999	90	75
1000	90	90

Table 3.1: Test conditions for different iliac wings

3.4.4 Positioning of the potted iliac wing below the fork

The potted wings are positioned below the fork. It is positioned in two different loading conditions. One is 75^o loading angle and another is 90^o loading angle. The 75^o and 90^o are the angles between the ASIS to AIIS line and the normal vector to the belt line. It is randomly assigned to the specimens in the experiment and those assigned are used here as well. Table 3.1 represents the varied test conditions assigned to wings.

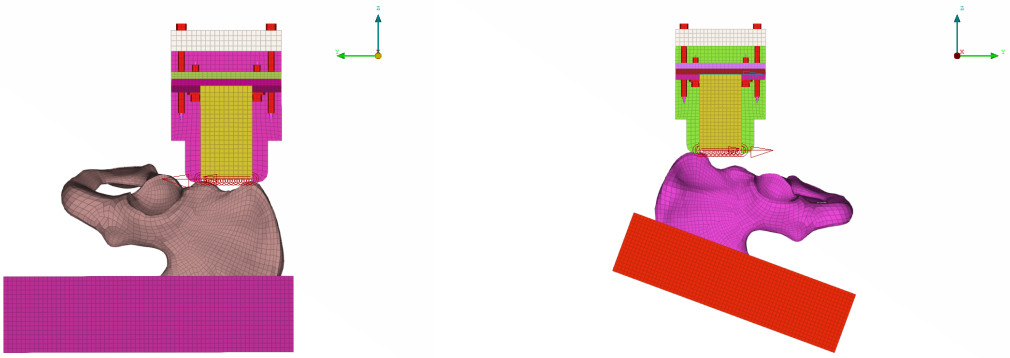

(a) Specimen 714 left (90^0 loading angle) (b) Specimen 715 right (75^0 loading angle)

Figure 3.14: Positioning of potted iliac wings

Figure 3.14 represents the two different loading conditions. To have consistent positioning for all the specimens, the 2021073 node number is chosen as the ASIS point for the right wings, and the 2006323 node number is chosen for the left wings. The distance between the ASIS point and the 67112 node number of the belt, located at the center of the belt, is maintained initially at 2 mm. Initially, the line connecting the ASIS and AIIS points is approximately maintained as a straight line. After this initial positioning, if the loading condition corresponds to a 75^o angle, the potted wing is rotated accordingly.

3.4.5 Contact definition

The automatic surface-to-surface contact definition is used to define the contact between the seat belt and the iliac wing. Here, the seat belt is chosen as the master and the iliac wing is chosen as the slave. A static coefficient of friction of 0.3 and a viscous damping coefficient of 20 is used. Optional card A is used for the contact, soft constraint option 2 i.e. segment-based contact is specified as the stiffness of the seat belt and the iliac wing material is different. In the segment-based contact option warped segment checking option is specified as, when the seat belt starts loading the wings, it wraps around the wing.

3.4.6 Global damping

The global damping is implemented following the same procedure as described earlier for the pretension phase. During the preload phase, all specimens are run without any damping. The specimen with the lowest frequency is selected to determine the critical damping, and this damping value is then applied to all the specimens. The critical damping is calculated as,

$$\text{critical damping} = \frac{4 \times \pi}{T} \tag{3.4}$$

T - Time period of the lowest frequency curve - 160 ms.

$$\text{critical damping} = \frac{4 \times \pi}{160} = 0.0785$$

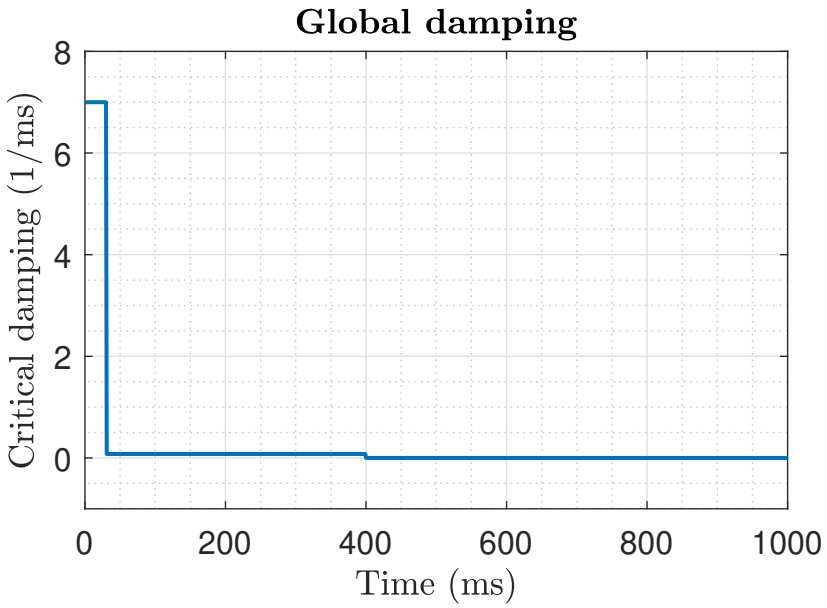

Figure 3.15: Global damping curve

Figure 3.15 represents the global damping curve used in the model. From 0 to 30 ms, the critical damping of 7 is used i.e. pretension-phase and from 30 to 400 ms 0.0785 is used i.e. pre-load phase.

3.4.7 Gravity load

In the experiment, as previously explained, to get a consistent starting position for the load the fork was positioned at 10 N pre-load at the start of every test. In the iliac wing tests it is achieved using a gravity load, instead of a prescribed velocity as in the calibration tests, since it became difficult to calculate the velocity needed to reach 10N for each case, due to the varying geometry. The gravity load is the acceleration given to the fork which is calculated as,

$$F = m \times a \tag{3.5}$$

F = 10 N = 0.01 kN, which should be achieved.
m = 6.62 kg, the mass of the fork

$$a = \frac{F}{m} = \frac{0.01}{6.62} = 0.00151 mm/ms^2$$

Due to variations in the geometry of each iliac wing, the interaction between the seat belt and the iliac wing also varies. As a consequence, the time required to reach a 10 N load varies between specimens. To ensure consistency in the analysis, the longest time taken by the specimen to reach the 10 N load is applied to all specimens. The longest time is found to be 400 ms, so the gravity load is applied for 400 ms for all the specimens.

3.4.8 Boundary conditions

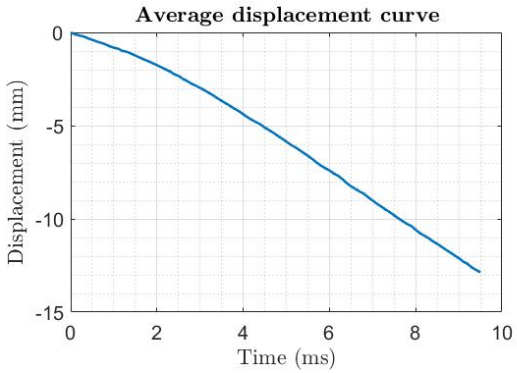

(a) Average displacement curve of 22 specimens

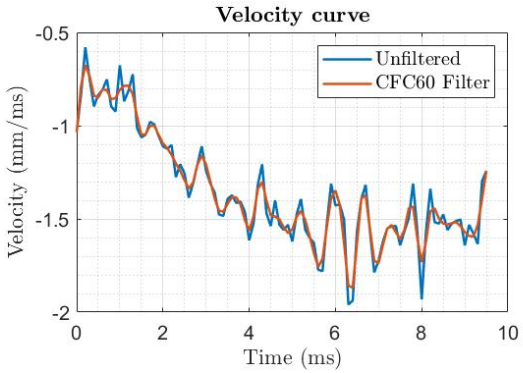

(b) Comparison of filtered and unfiltered velocity curve

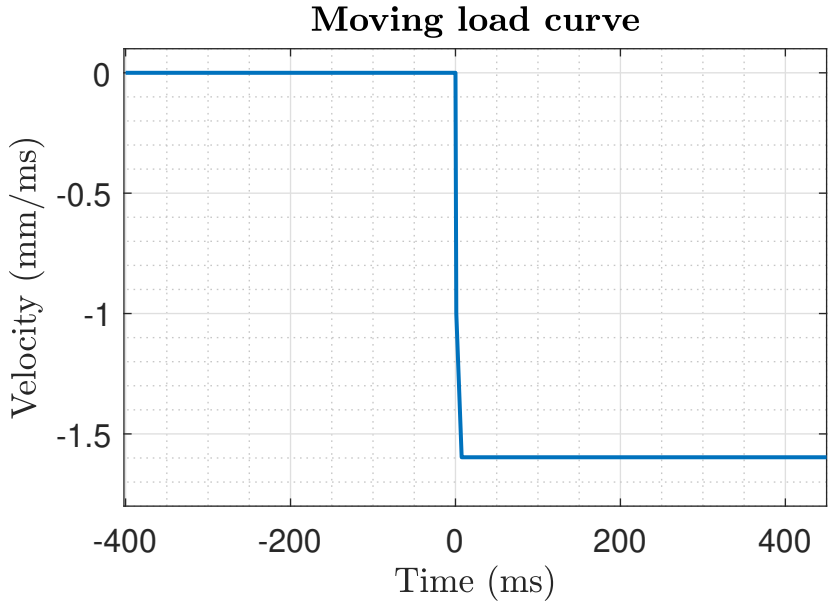

Figure 3.17: Load curve for translational z-direction

The boundary condition explained for the seat belt characterization test is used in the iliac wing test as well except for the translational z movement. The translational z movement is given as the velocity curve, which is obtained from the experiments. The displacement data for all 22 specimens were available and the average of 22 specimens was taken 3.16a. The average displacement curve is then differentiated with respect to the time vector, due to the noise in the data cfc60 filter is used to remove the noise from the data which can be seen in figure 3.16b. The filtered curve is simplified in bi-linear form which can be seen in the figure 3.17 and that curve is used in ANSA for the translational z-motion. The birth time of the curve is given as 400 ms because until 400 ms gravity load is applied and then this curve starts acting. The total time of the simulation is 450 ms.

3.5 Generation of the Injury Risk Function

Different measures of stress and strain data like maximum principal strain, minimum principal strain, effective strain, effective plastic strain, and maximum shear stress are extracted from the iliac wing simulations, at the time when the force reaches the force which was recorded as the fracture force in the experiment and saved in .csv format. Age, stature, and body mass index (BMI) are used as the initial covariates. The Cox regression model was used to select the covariate which was found to be significant. The covariates with a p-value lesser than 0.05 are selected. The library "survival" is used in the R package to perform the survival analysis. Different distributions like Weibull, lognormal, and log-logistic are used. The distribution with the lowest AIC value is chosen to generate an IRF and a 95% confidence interval is plotted for the selected distribution.

There are a total of 22 iliac wings i.e, 22 data points. 18 data points are exact

censored,2 are left censored and 2 are right censored. 2 left censored data points are neglected in the study. So with 20 data points the IRF is generated for both the surface matched and the landmarked iliac wings. But from the statistical point of view, treating the left and right wings as separate data points is incorrect since they are dependent, so the average of the left and right iliac wings are considered. The left iliac wing data for two cases contain left censored values, and for those specific wings, the average is not calculated and the data from the right iliac wing is considered. The data points from 20 it is reduced to 11. For the 11 data points the IRF is generated for all the strain measures for the surface matched iliac wings. Further to check the robustness of the IRFs and the sensitivity to the weakest PMHSs the three lowest strain values are removed gradually and the effective strain is used as a measure to generate the IRFs for this investigation.

4

Results

In this section, the results of the seat belt characterization, iliac wing tests, comparisons of the FE model against experimental results, and Injury Risk Functions for the different measures are presented.

4.1 Seat belt characterization test

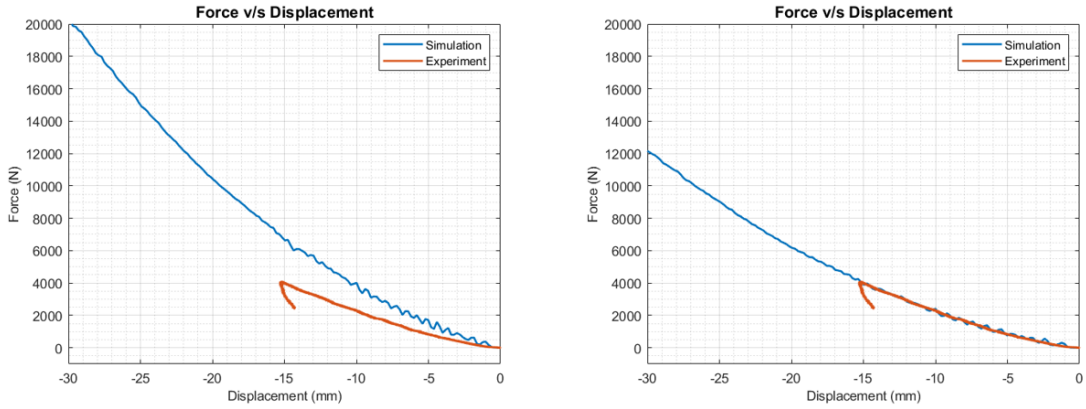

(a) Force v/s displacement graph with original parametrs

(b) Force v/s displacement graph with changed parameters

Figure 4.1: Comparison of the FE model and the experimental results

Figure 4.1 represents the force-displacement relationship between the simulation and experimental results. In Figure 4.1a, the graph represents the case where the bolt pretension force is set to 2.8 kN and the seat belt stiffeness is at 20% strain at 18.268 kN. However, the stiffness of the finite element (FE) model was observed to be higher than the experimental results when using the baseline values.

After the calibration study, it was found that when the pretension force was set to 1.8 kN and the seat belt is at 20% strain at 10.96 kN, the stiffness of the FE model matched the experimental results. These specific values were adopted for the subsequent iliac test as well.

4.2 Iliac wing test

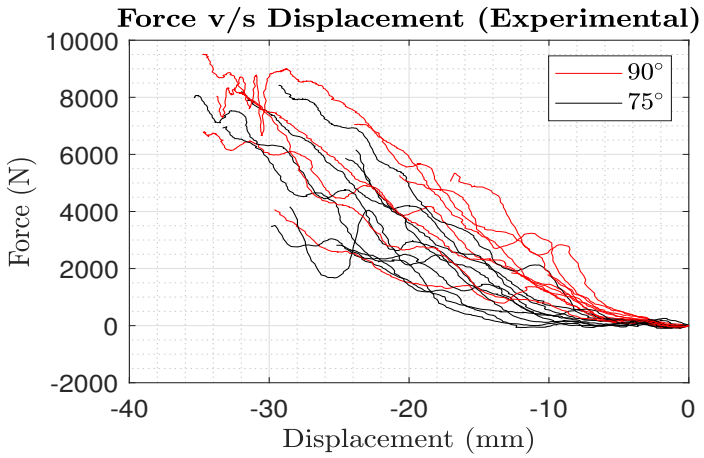

Figure 4.2: Force v/s displacement graph for experimental results

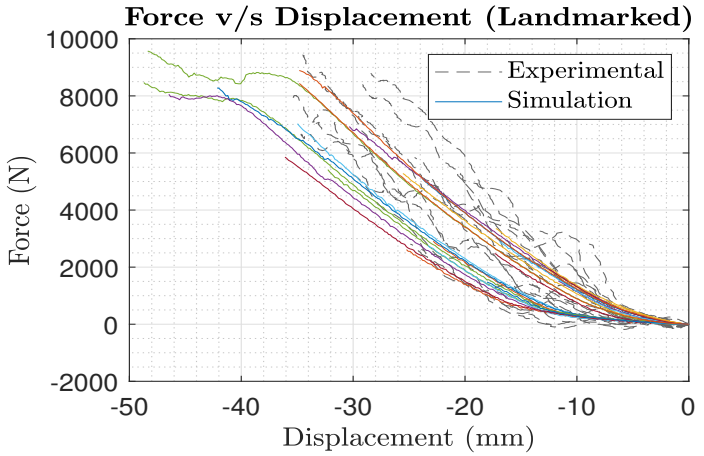

Figure 4.3: Comparison of the FE model and experimental for landmarked wings

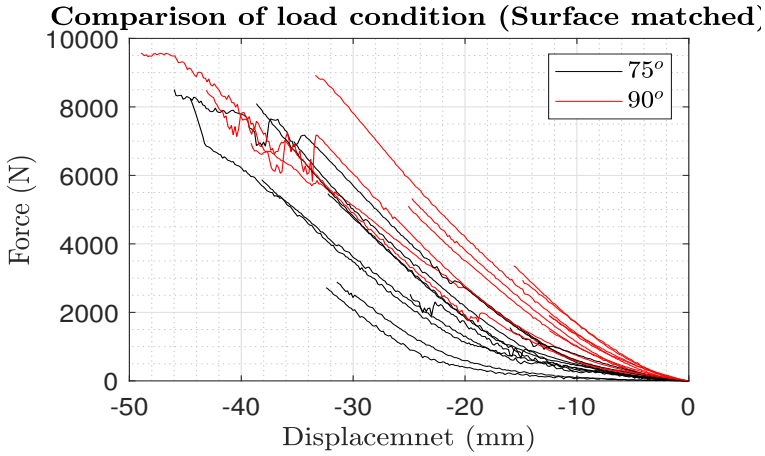

Figure 4.4: Force v/s displacement graph for FE modelled surface matched wings

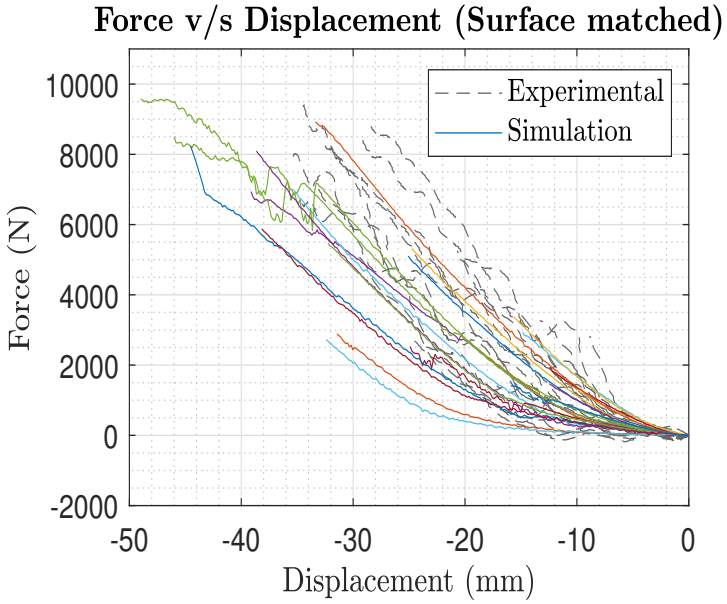

Figure 4.5: Comparison of the FE model and experimental for landmarked wing

Figure 4.3 and 4.5 represent the force and displacement graph for the landmarked iliac wing simulations and surface-matched iliac wing simulations against the experimental iliac wing tests. The grey line represents the experimental results and the coloured line represents the simulation results. The experimental results are taken from the time when the fork starts the downward movement to the time of the first event (indication of fracture). The simulation results are taken from the 400 ms time (from the start of the translational z boundary condition) to the time when it reaches the force which was recorded in the experiment. To establish the starting point with zero force and position, both the force and displacement vectors are subtracted from the initial value.

The landmarked specimens simulation results are divided into two significant groups showing the two different loading conditions. The stiffer group represents the 90^o loading condition and the weaker group represents the 75^o loading condition. The same trend is seen in the experimental results 4.2 and surface-matched results 4.4 also but with greater overlap.

Figure 4.6 and 4.7 represent the contour plots for the cortical bones and trabecular bones respectively. The contour plots are extracted at the time when the force reaches the recorded first event of the fracture from the experiment. For different specimens, the region of the stress concentration varies as seen in the figures.

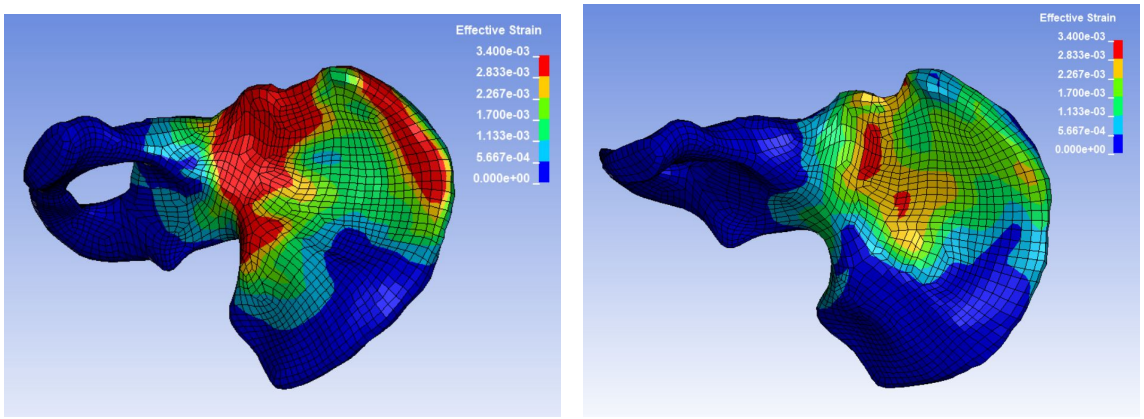

(a) Specimen:713R (b) Specimen:999R

Figure 4.6: Effective strain contour plots for the cortical bone

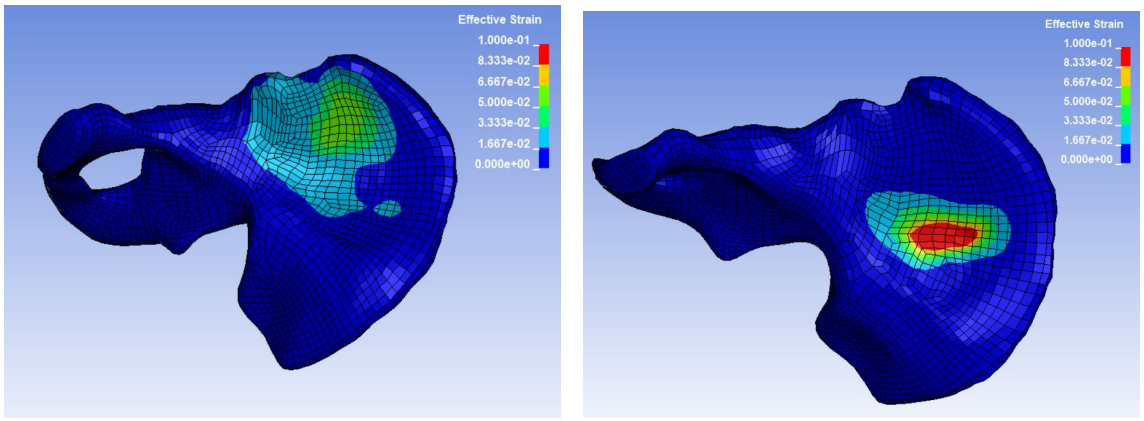

(a) Specimen:713R (b) Specimen:999R

Figure 4.7: Effective strain contour plots for the trabecular bone

4.3 Injury Risk Functions

In this section, IRF for the different measures are presented.

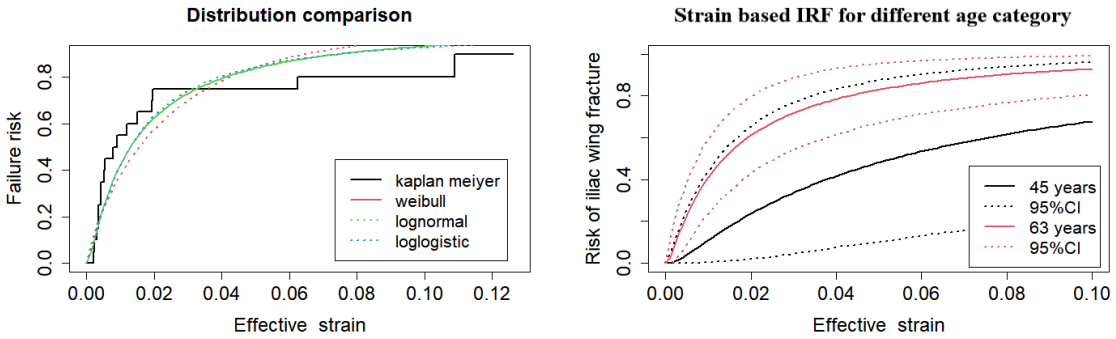

(a) Comparison of different distribution (b) IRF for the different age category

Figure 4.8: IRFs for different distribution and age category

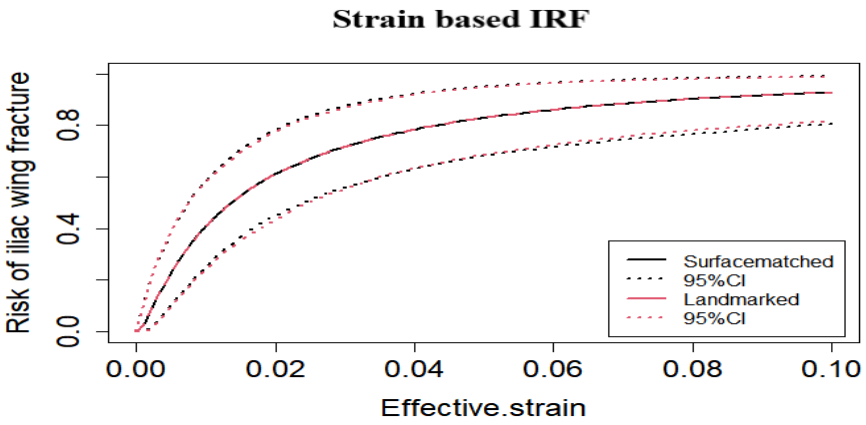

Figure 4.9: Comparison of the surface matched and landmarked wings

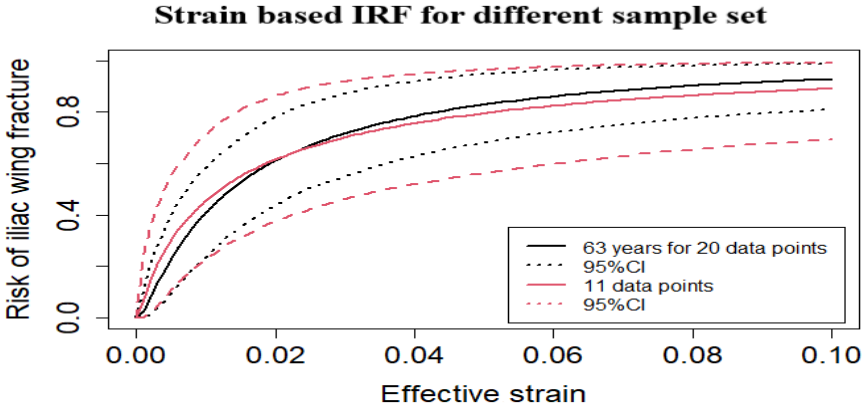

Figure 4.10: IRF for the 20 and 11 datasets

Figure 4.8a represents the survival analysis of the 20 data points with different distributions for the effective strain measure.

The log-normal distribution had the lowest AIC score and hence was used when generating the IRF. Figure 4.8b represents the IRF for the effective strain when age is considered as a covariate. 63 years is the average age of the data set used, and 45 years is considered as the average adult age of the whole population. As it is seen in the figure the confidence interval band for the 63 years is narrower, while 45 years have a wider band.

Figure 4.9 represents the comparison of the landmarked wings and the surface matched wings for the effective strain measure. Even for the landmarked wings, the age was found to be significant, and the lognormal distribution had the lowest AIC. As 63 years is the average age of the data, it is used to plot the IRF for comparison. As it is seen in the figure, for both the data, the IRF overlaps on each other and only the 95% CI band is a little narrower compared to the surface matched wings. As there is not much difference between the IRFs, for further analysis surface matched data is used as it is more accurate in the geometry of the cadaver's iliac wings.
Figure 4.10 represents the comparison of the IRF for the 20 and 11 data points. For the 11 data points, no covariates were significant for effective strain measure, and log-normal distribution had the lowest AIC score. The IRF for both the data sets looks similar, but the 95% CI band for the average data set is wider compared to the other data set.

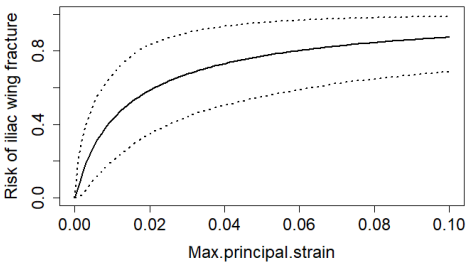

(a) IRF for Max principal strain

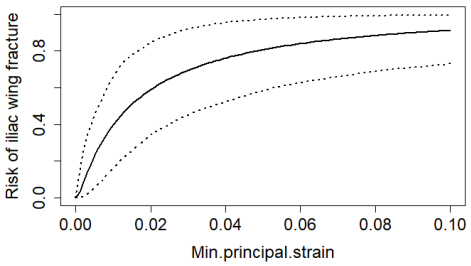

(b) IRF for Min principal strain

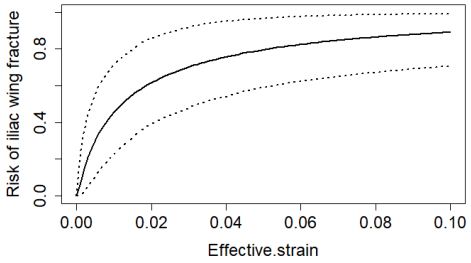

(c) IRF for Effective strain

Figure 4.11: IRF for different measures for the cortical bone

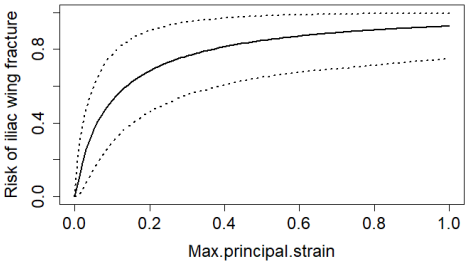

(a) IRF for Max principal strain

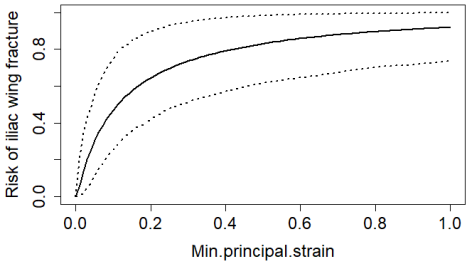

(b) IRF for Min principal strain

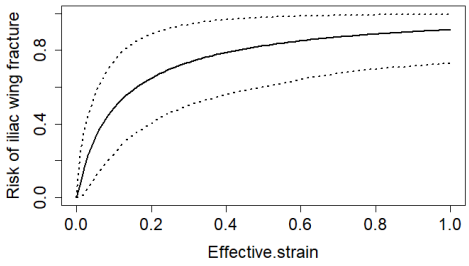

(c) IRF for Effective strain

Figure 4.12: IRF for different measures for the trabecular bone

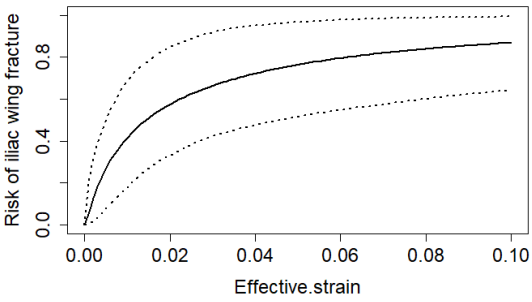

(a) IRF for the Effective stain for the 10 data points

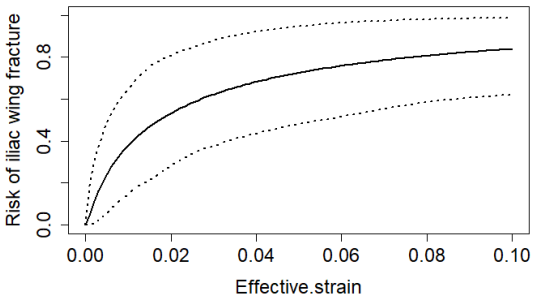

(b) IRF for the Effective strain for the 9 data points

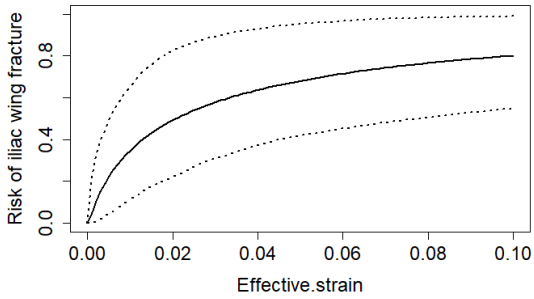

(c) IRF for the Effective strain for 8 data points

Figure 4.13: IRF's for the Effective strain when the data points are removed

Figure 4.11 and 4.12 shows the IRF for the cortical and trabecular bone respectively. For all the measures, no covariates were found to be significant and lognormal distribution was used since this had the lowest AIC score for all the measurements.

For further analysis effective strain of the cortical bone is considered. Figure 4.13a, 4.13b, and 4.13c represent the IRF for the effective strain when the lowest effective strain is removed. As it is seen, as the lowest data set is removed the band for the confidence interval increases.

5

Discussion

The objective of this thesis work was to re-create an iliac wing loading experiment in simulations using a FE model and to create an IRF for the same scenario. The fork FE model was validated with the experimental results to check the accuracy of the model, which is discussed in the following section. Due to the lack of experimental results in this field, the generated IRF will be useful as a starting point for further research, but it should not be directly implemented by industry in the development of new seat belt designs.

5.0.1 Calibration of simulation model

When the simulation was carried out with the baseline parameters, the resulting stiffness was greater compared to that of the experiment, as seen in figure 4.1a. This might be due to a lot of unknown factors in the experiment. One is slippage of the seat belt in the clamping plates. When the bolt is pre-tensioned and comes in contact with the aluminium bar there will be slippage of the seat belt, and the length of the slippage is unknown. Another is the pre-tension torque which is given in the experiment, but due to the complexity of the geometry, the actual pretension force transferred to the bolts is unknown. After the pretensioning of the bolts, the start time of the experiment is unknown, so the seat belt might have experienced creep, but the creep effect is unknown. Also, there is a deformation in the clamping plates which was visible in the videos of the experiment, but the magnitude of the deformation is difficult to judge. Finally, the belt friction against the belt fork is also unknown. Due to all these unknowns, the stiffness of the fork might be more than the experiment and due to this the calibration of the FE model was required. In this project, the calibration parameters considered were bolt pre-tension force and the seat belt stress-strain characteristics. This means that the unknown effects listed above are grouped into these two parameters, which is a simplification compared to reality. This might have the implications that the actual results from the reality can't be captured but it gives a good match to the experimental results. The other things to consider while trusting the calibration results are that the actual specimen i.e, the iliac wing is not smooth and round, and the loading for the specimens are done beyond the loading range of the calibration results.

5.0.2 Simulation results

In figure 4.3 and 4.5, the landmarked wings have the tighter band with the experimental results but the surface matched results have the same overlap trend for the varying loading condition as the experimental results. But the IRF suggested that the both results predicted the same risk curve. So the question is, is it required to do the additional work for the surface matched specimens, if the end result is generating an IRF the additional work can be excluded.

However, in both the results but more obvious in surface matched results, the transition from the initial weak to the stiff response is captured well. This might be because, in the experiment, the wings are not cleaned completely and some skin is left on the bone which is not possible to capture in the simulation. It also could be that the validated belt stiffness effects the edge loading. It is seen that the weakest subject has the most extreme edge effect due to the 75 degree angle and there is a steep slope from ASIS to AIIS point compared to other geometries.

The exact type of fracture is unknown from the simulation results as each specimen fails differently. Some of the specimens fail from shear, some from compression and some from bending. From figures 4.6 and 4.7, it is clearly seen that the stress concentration regions are different and they both undergo different types of failure which was evident in the videos.

5.0.3 Injury Risk Function

The iliac wing tests are considered as separate data points and plotted with age as a covariate seen in figure 4.8b. It is seen that for the 45 years age, the confidence band is wider. This is because, in the data sets used in the experiment, the lowest age is 50 years and 45 years is an extrapolation outside of the data range.

For further analysis, the average of left and right wing is considered [41] because it is recommended to have only one IRF per body region [27] and also it violates the statistical assumption due to the dependency between samples. To avoid dependency, either the left or right wings could have been chosen, but by doing this, the complete data of one wing will be unused. So the average was taken, in this most of the data will be considered but still while averaging some data will be lost. There are different methods to deal with the dependency of the data which has to be explored in future work. Some of the different methods which can be used to deal with the available data are using the frailty model [43] or the generalised estimating equation, which uses the clustering of the data to deal with the dependency [42]. In our case, the right and left wing of the specimen can be treated as a cluster.

The effective strain is calculated using the deviatoric strains, as the fracture type is unknown the effective strain is a good measure for calculating the IRFs. In the figures 4.13a,4.13b, and 4.13c, the lowest strain is removed gradually because we found samples that fractured very early, way before the plastic zone of the material. This was an attempt to check how the 50% risk of fracture and the confidence band

changes. This was motivated by the fact that the specimens with the lowest strain had all died from the disease of congestive heart failure. Individuals with this disease have a high chance of having osteoporosis [32]. Osteoporosis is a condition where the bone mineral density is less compared to the normal population [37]. The bones with less bone mineral density will be fragile and brittle, so it is more prone to fracture. As it is seen in the images 4.13a, 4.13b, and 4.13c , the strain value for the 50% risk increases by 40% when these specimens were removed gradually.

5.0.4 Conclusion

This Master's Thesis project involved the generation of multiple IRFs using different measures and datasets. However, a conclusive single IRF suitable for practical applications could not be determined. The exploration of various IRF development approaches was conducted, providing valuable insights for future work. Further efforts are required to generate the IRF, such as considering left-censored data and exploring alternative statistical methods capable of handling data dependencies. Additionally, more experiments need to be conducted to establish a trustworthy IRF for practical applications in this field.

The FE model resembles the actual experiment, and future research could involve incorporating the seat belt looped in the clamping plates to assess its impact on the existing results. It is recommended to avoid such complexities in future experiments, as it would simplify the modelling process and enhance its reliability. Overall, this study makes a significant contribution to future research that should be conducted in this area.

Bibliography

[1] Center for disease control and prevention."Road Traffic Injuries and Deaths—A Global Problem" [Online]. Available:https://www.cdc.gov/injury/features/global-road-safety/index.html.(Accessed: 12-Apr-2023)

[2] WHO."Road traffic injuries"[Online].Available :https://www.who.int/news-room/fact-sheets/detail/road-traffic-injuries.(Accessed: 12-Apr-2023)

[3] Brake the road safety charity. " GLOBAL ROAD SAFETY STATISTICS" [Online]. Available:https://www.brake.org.uk/get-involved/take-action/mybrake/knowledge-centre/global-road-safety. (Accessed: 12-Apr-2023)

[4] UN."Road Safety-Considerations in Support of the 2030 Agenda for Sustainable Development"[Online]. Available: https://unctad.org/system/files/official-document/dtltlb2017d4en.pdf.(Accessed: 12-Apr-2023)

[5] Smart city Sweden."Vision Zero – Reducing Road Traffic Casualties and Injuries" [Online]. Available: https://smartcitysweden.com/best-practice/408/vision-zero-reducing-road-traffic-casualties-and-injuries/: :text=Vision

[6] Mónica Diez and Julio Abajo and Jesús Vázquez de Prada and Alberto Negro and M. Teresa Fernández, "Sitting posture influence in autonomous vehicles for the evaluation of occupant safety in side impact", Safety Science, March 2023, Volume 159. DOI: https://doi.org/10.1016/j.ssci.2022.106002

[7] Rawska, K., Gepner, B., Kerrigan, J. R. "Effect of various restraint configurations on submarining occurrence across varied seat configurations in autonomous driving system environment", Traffic Injury Prevention, 2021, pp.128-133. DOI: 10.1080/15389588.2021.1939872

[8] N.Ottosen and H.Petersson, "Introduction to the Finite Element Method". Prentice Hall, 1992.

[9] J.N.Reddy, "Introduction to the Finite Elemenet Method 4th edition". ISBN: 9781259861901

[10] Pelvis anatomy [Online]. Available:https://www.orthobullets.com/recon/12768/pelvis-anatomy.(Accessed: 15-May-2023)

[11] Elements [Online]. Available : https://www.dynasupport.com/tutorial/ls-dyna-users-guide/elements.(Accessed: 15-May-2023)

[12] "Importance of Aspect Ratio in Finite Element Analysis and its calculation for 2D Elements"[Online]. Available: https://www.engmorph.com/2d-element-aspect-ratio-calc.(Accessed: 16-May-2023)

[13] "Skewness Calculation for 2D Elements"[Online]. Available: https://www.engmorph.com/skewness-finite-elemnt.(Accessed: 16-May-2023)

[14] "Warp angle"[Online]. Available: https://support.ptc.com/help/creo/creopma/r9.0/usascii/index.htmlpage/simulate/simulate/fwarpangle.html.(Accessed: 16-May-2023)

[15] R.B.Martin, D.B.Burr, N.A.Sharkey, and D.P.Fyhrie,"Skeletal Tissue Mechanics".2015,vol.Second Edition,ISBN: 978-1-4939-3002-9.

[16] "Elements"[Online]. Available: https://www.dynasupport.com/tutorial/ls-dyna-users-guide/elements. (Accessed: 23-May-2023)

[17] Erik Brynskog, Johan Iraeus, Bengt Pipkorn, Johan Davidsson, "Population variance in Pelvic Response to Lateral impacts- A Global Sensitivity Analysis IRC - 22-34 IRCOBI". URL:https://research.chalmers.se/publication/532559

[18] Jason L. Forman, Francisco J. Lopez-Valdes, Sonia Duprey, Dipan Bose, Eduardo del Pozo de Dios, Damien Subit, Tim Gillispie, Jeff R. Crandall, Maria Segui-Gomez," The tolerance of the human body to automobile collision impact - A systematic review of injury biomechanics research,1990-2009". Accidental Analysis and Prevention, vol 80, 1 July 2015, pp.7-17. DOI:https://doi.org/10.1016/j.aap.2015.03.004

[19] KenjiInabaPhilip, WSharkeyDavid, J.GStephenDonald, ARedelmeierFrederick, DBrenneman. "The increasing incidence of severe pelvic injury in motor vehicle collisions".International journal of the care of the injured, August 2004, vol 35, issue 8, pp.759-765. DOI: https://doi.org/10.1016/S0020-1383(03)00308-5

[20] Ashley A. Weaver, Ryan T. Barnard, Patrick D. Kilgo, R. Shayn Martin, and Joel D. Stitzel. "Mortality-based quantification of injury severity for frequently occurring motor vehicle crash injuries. Paper presented at the Annals of Advances in Automotive Medicine". Ann Adv Automot Med, September 2013, pp.235-246. URL: https://www.scopus.com/record/display.uri?eid=2-s2.0-84888087277origin=inwardhttps://www.scopus.com/record/display.uri?eid=2-s2.0-84888087277origin=inwardhttps://www.scopus.com/record/display.uri?eid=2-s2.0-84888087277origin=inward

[21] Kai-Uwe Schmitt . Peter F. Niederer Duane S. Cronin · Markus H. Muser Felix Walz. "Trauma Biomechanics - An introduction to injury biomechanics ". Springer Heidelberg New York Dordrecht London, Fourth edition. DOI: 10.1007/978-3-642-53920-6 .

[22] Uriot, Jérôme;Baudrit, Pascal; Potier, Pascal; Trosseille, Xavier; et al," Investigations on the Belt-to-Pelvis Interaction in Case of Submarining", Stapp Car Crash Journal, November 2006, vol 50, pp.53-73. DOI: 10.4271/2006-22-0003.

[23] T G Clark, M J Bradburn, S B Love, and D G Altman, "Survival Analysis Part I: Basic concepts and first analyses", Br J Cancer, July 2003, pp.232-238.DOI: 10.1038/sj.bjc.6601118

[24] Vittinghoff E, Glidden DV, Shiboski SC, McCulloch CE."Regression Methods in Biostatistics". New York: Springer New York; 2005

[25] Akaike information criterion[Online]. Available: https://en.wikipedia.org/wiki/Akaike informatiocriterion. (Accessed: 30-May-2023)

[26] Norbert Praxl, "HOW RELIABLE ARE INJURY RISK CURVES?", PDB – Partnership for Dummy Technology and Biomechanics Germany,2011.URL: https://www-esv.nhtsa.dot.gov/Proceedings/22/files/22ESV-000089.pdf

[27] Audrey Petitjean, Xavier Trosseille, Norbert Praxl, David Hynd, Annette Irwin."Injury Risk Curves for the WorldSID 50th Male Dummy", Stapp Car Crash Journal, October 2012, vol 56, pp. 323-347. DOI: 10.4271/2009-22-0016

[28] Confiedence interval in statistics[Online]. Available:https://www.simplypsychology.org/ confidence-interval.html. (Accessed: 30-May-2023)

[29] Jiang, B., Ren, H., Zhu, F., Chou, C., Bai, Z."A preliminary study on the restraint system of self-driving car", SAE Technical Papers,2020, pp.2401-2410, DOI: https://doi.org/10.4271/2020-01-1333.

[30] Rachel Richardson, John-Paul Donlon, Mohan Jayathirtha, Jason L. Forman, Greg Shaw, Bronislaw Gepner, Jason R. Kerrigan,Martin Östling, Krystoffer Mroz, Bengt Pipkorn."Kinematic and Injury Response of Reclined PMHS in Frontal Impacts", Stapp Car Crash Journal, November 202, vol 64, pp.83-153, DOI:10.4271/2020-22-0004.

[31] David Moreau1, John Paul Donlon, Aida Chebbi, Mohan Jayathirtha, Sara Sochor, Brian Overby, Rachel Richardson, Bronislaw Gepner, Jason Forman, Martin Östling, Jason Kerrigan. "A Methodology to Replicate Lap Belt Loading Conditions from a Sled Impact Test in a Non-Impact Dynamic Environment on Whole-Body Postmortem Human Subjects", IRCOBI, September 2021. DOI: http://www.ircobi.org/wordpress/downloads/irc21/pdf-files/2136.pdf

[32] Wenmin Xing, Xiaoling Lv, Wenyan Gao, Jirong Wang, Zhouxin Yang, Sanying Wang, Jing Zhang, Jing Yan."Bone mineral density in patients with chronic heart failure: a meta-analysis", Clinical intervention in aging, February 2018, vol 13, pp.343-353. DOI:10.2147/CIA.S154356

[33] Katarzyna Rawska, Bronislaw Gepner, David Moreau, Jason R Kerrigan. "Submarining sensitivity across varied seat configurations in autonomous driving system environment", Traffic injury prevention, October 2020, vol 21, pp.1-6. DOI: 10.1080/15389588.2020.1791324

[34] Stéphane Couturier, Jacques Faure, Ricardo Satué, Joaquim Huguet, Julien Hordonneau, "PROCEDURE TO ASSESS SUBMARINING IN FRONTAL IMPACT",20th International Technical Conference on the Enhanced Safety of Vehicles (ESV), June 2007.

[35] "Paving the Way for a Smarter, Safer Future of Autonomous Vehicles",[Online]. Available: https://redshift.autodesk.com/articles/future-of-autonomous-vehicles. (Accessed: 05-June-2023)

[36] Elise F. Morgan, Ginu U. Unnikrisnan, Amira I. Hussein."Bone Mechanical Properties in Healthy and Diseased States", June 2019. DOI: 10.1146/annurev-bioeng-062117-121139

[37] Georg Osterhoff, Elise F. Morgan, Sandra J. Shefelbine, Lamya Karim, Laoise M. McNamara, and Peter Augatg."Bone mechanical properties and changes with osteoporosis", June 2017. DOI: 10.1016/S0020-1383(16)47003-8

[38] Mikael Dahlgren, Abhiroop Vishwanatha, Anurag Soni, Klas Engstrand, Jimmy Forsberg, Isheng Yeh. "Belt Modelling in LS-DYNA", 16th International LS-DYNA User's Conference. Available: https://www.dynalook.com/conferences/16th-international-ls-dyna-conference/aerospace-01-2/t1-2-b-aerospace-148.pdf.

[39] Erik Brynskog, Johan Iraeus, Matthew P.Reed, Johan Davidsson."Predicting pelvis geometry using a morphometric model with overall anthropometric variables".Journal of Biomechanics, September 2021. DOI: 10.1016/j.jbiomech.2021.110633

[40] Smooth-cast 300 series. Available: https://www.smooth-on.com/tb/files/Smooth-Cast300q,300,305310.pdf

[41] Richard W. Kent, Kristoffer Mroz, Bengt Pipkorn, Ola Bostrom, Maria Segui-Gomez. "Predicting Rib Fracture Risk With Whole-Body Finite Element Models: Development and Preliminary Evaluation of a Probabilistic Analytical Framework", European Center for Injury Prevention, October 2012, vol 56. DOI:http://worldcat.org/issn/19432461

[42] "Getting Started with Generalized Estimating Equations"[Online]. Available: https://data.library.virginia.edu/getting-started-with-generalized-estimating-equations/. (Accessed: 05-June-2023).

[43] Marco Munda, Federico Rotolo, Catherine Legrand."parfm: Parametric Frailty Models in R",Journal of Statistical Software, November 2012, Vol 51.DOI: https://www.jstatsoft.org/index.php/jss/article/view/v051i11/651.

[44] Tümay Sözen,Lale Özışık,and Nursel Çalık Başaran."An overview and management of osteoporosis", European journal of Rheumatology, March 2017, vol 4,pp 46-56. DOI:10.5152/eurjrheum.2016.048.

[45] Bart Clarke,"Normal Bone Anatomy and Physiology",Clin J Am Soc Nephrol, November 2008,vol 3. DOI: 10.2215/CJN.04151206

[46] Jorge A.C. Ambrósio,Marta Carvalho,João Milho,Susana Escalante's,João Milho. "A validated railway vehicle interior layout with multibody dummies and finite element seats models for crash analysis", Multibody System Dynamics 54(2),February 2022. DOI:10.1007/s11044-021-09794-w.

[47] Types Of Fractures[Online], Available:https://www.flickr.com/photos/. (Accessed: 12-Dec-2023)

[48] Ligaments of pelvis [Online], Available: https://wikimedia.org/File:Ligaments of Pelvis.jpg (Accessed: 12-Dec-2023)

[49] Hip bone [Online], Available: https://commons.wikimedia.org/wiki/File:808Hip Bone.jpg (Accessed: 12-Dec-2023)

[50] Hybrid II and Hybrid III crash test dummies [Online], Available: https://www.flickr.com/photos/nationalmuseumofamericanhistory/4796774241 (Accessed: 12-Dec-2023)

[51] David Moreau, Pavel Chernyavskiy, Sara Sochor, Bronislaw Gepner, Jason Forman, Martin Östling, Jason R Kerrigan."Development of an Injury Risk Function for the Anterior Pelvis Under Frontal Lap Belt Loading Conditions", Ann Biomed Eng 51(9),2023 Sep. DOI: 10.1007/s10439-023-03244-8.

[52] Rachel Richardson, John-Paul Donlon, Bronislaw Gepner, Jason Forman, Jason Hallman, Jason Kerrigan."The Effects of Recline Angle and Restraint Geometry on Lap Belt–Pelvis Interaction for Above-Normal BMI Motor Vehicle Occupants", Ann Biomed Eng 51, 2566–2578 (2023). https://doi.org/10.1007/s10439-023-03302-1

[53] R.Richardson, M.Jayathirtha, J.P.Donlon, J.L. Forman, B.Gepner, M.Ostling, K.Mroz, B.Pipkorn, J.R. Kerrigan, "Pelvis Kinematics and Injuries of Reclined

Occupants in Frontal Impacts", IRCOBI. IRC-20-60, 2020. DOI: 10.4271/2020-22-0004

DEPARTMENT OF SOME SUBJECT OR TECHNOLOGY
CHALMERS UNIVERSITY OF TECHNOLOGY
Gothenburg, Sweden
www.chalmers.se

CHALMERS
UNIVERSITY OF TECHNOLOGY